

Thermoelectric Properties of Materials Based on Double Filled Type-I Clathrates

by

Rafay Uz Zaman Shams

*A thesis
presented to the University of Waterloo
in fulfillment of the
thesis requirement for the degree of
Master of Science
in
Chemistry*

Waterloo, Ontario, Canada, 2015

© Rafay Uz Zaman Shams 2015

Author's Declaration

I hereby declare that I am the sole author of this thesis. This is a true copy of the thesis, including any required final revisions, as accepted by my examiners.

I understand that my thesis may be made electronically available to the public.

Rafay Uz Zaman Shams

Abstract

Energy consumption is at an all-time high. However, abundant energy is lost as waste heat. Thermoelectric materials are of interest within the scientific community due to their ability to convert waste heat into useful electricity. Their application is limited though because of low efficiency. Type-I clathrates were discovered as potentially high performing thermoelectric materials after Slack proposed his PGEC (Phonon-Glass-Electron-Crystal) concept in 1995. Type-I clathrates, which are semiconducting caged structures, have remarkably low thermal conductivity due to scattering of phonons by caged atoms which act as rattlers. $\text{Ba}_8\text{Ga}_{16}\text{Ge}_{30}$ has emerged as the leading candidate for clathrates.

Here we investigate the effects of double filling the clathrate cages with lanthanide (Ln) elements along with Ba on the thermoelectric properties of Type-I clathrates with the formula $\text{Ba}_{8-x}\text{Ln}_x\text{Ga}_{16}\text{Ge}_{30}$. Ln elements, La and Eu, have been successfully used as substitute elements. $\text{Ba}_{8-x}\text{La}_x\text{Ga}_{16}\text{Ge}_{30}$ and $\text{Ba}_{8-x}\text{Eu}_x\text{Ga}_{16}\text{Ge}_{30}$ have been synthesized successfully. All the compounds have been prepared by solid-state reaction. Powder X-ray diffraction (PXRD) results indicate that the samples are pure phase Type-I clathrates after initial synthesis. Clathrates crystallize in $Pm\bar{3}n$ space group. All clathrates were found to be *n*-type semiconductors. Temperature dependencies of the electrical conductivity, σ , Seebeck coefficient, S , and thermal conductivity, κ , have been measured in the range from 300 K to 850 K for several La and Eu double filled clathrates.

La inclusion causes an increase in the thermoelectric figure-of-merit of up to 8% with $\text{Ba}_{7.9}\text{La}_{0.1}\text{Ga}_{16}\text{Ge}_{30}$ displaying a ZT of 0.66 at 780 K. Eu inclusion causes an increase in figure-of-merit up to 13% with $\text{Ba}_{7.8}\text{Eu}_{0.2}\text{Ga}_{16}\text{Ge}_{30}$ displaying a ZT of 0.69 at 770 K.

Acknowledgments

I would like to thank my supervisor, Professor Holger Kleinke, for all the help, advice, support and encouragement he provided throughout my Masters studies at University of Waterloo. I have learned a lot from him over the years and his advice has always helped me to move my project along.

I would thank Dr. Jalil Assoud for his help especially with single crystal analysis. I would also like to thank all my group members, past and present, for all their help. Special thanks to Nader Farahi, Quansheng Guo, Tigor Mihaljevic and Katja Kleinke for their help and support in lab matters. Mohamed Oudah, Nhi Truong, Nagaraj Nandihalli, Raj Sankar, Yixuan Shi and other members of the Kleinke group have been really helpful too.

I would thank my committee members, Professor Richard Oakley and Professor Linda Nazar.

Funding from Natural Sciences and Engineering Research Council of Canada is appreciated.

Finally, I would thank my family for their continued support.

Table of Contents

Contents

Author's Declaration	ii
Abstract	iii
Acknowledgments.....	iv
Table of Contents.....	v
List of Figures	viii
List of Tables	x
Glossary.....	xi
1. Introduction	1
1.1 Thermoelectric Effects History.....	1
1.2 Thermoelectric Applications	3
1.3 Thermoelectric figure-of-merit.....	5
1.4 Seebeck Coefficient.....	6
1.5 Electrical Conductivity.....	6
1.6 Thermal Conductivity.....	7
1.7 Material Selection	8
2. Literature Review	10
2.1 Bi ₂ Te ₃	10
2.2 PGEC Concept.....	11
2.3 Skutterudites.....	12
2.4 Clathrates	12
2.4.1 Clathrate Types	13
2.4.2 Type I clathrates.....	15
2.4.3 Clathrate Literature Review	18
3. Sample Preparation and Analysis.....	21
3.1 Synthesis	21
3.2 Powder X-ray Diffraction (PXRD).....	23
3.3 Single Crystal.....	24
3.5 SEM with EDX.....	26
3.6 EPMA.....	27

3.7 Hot Press	29
3.8 Thermal Conductivity Measurement	30
3.9 Seebeck Coefficient and Electrical Conductivity Measurement	32
4. Lanthanum filled clathrates	34
4.1 Synthesis	34
4.2 XRD Analysis.....	34
4.3 EDX Analysis	37
4.3.1 $x = 0.1$	37
4.3.2 $x = 0.2$	39
4.4 EPMA.....	41
4.4.1 $x = 0.1$	41
4.4.2 $x = 0.2$	41
4.5 Physical Property Measurements	42
4.5.1 Thermal Conductivity.....	42
4.5.2 Electrical Conductivity.....	44
4.5.3 Seebeck coefficient	45
4.5.4 Power Factor	48
4.5.5 Figure-of-merit.....	49
4.6 Conclusion.....	51
5. Eu containing clathrates.....	52
5.1 XRD Analysis.....	53
5.1.1 PXRD Analysis.....	53
5.1.2 Single Crystal.....	55
5.2 EDX.....	58
5.2.1 $x = 0$	58
5.2.2 $x = 0.1$	59
5.2.3 $x = 0.2$	61
5.2.4 $x = 0.3$	62
5.3 EPMA.....	63
5.3.1 $x = 0$	63
5.3.2 $x = 0.2$	63
5.3.3 $x = 0.5$	64

5.4 Physical Property Measurements	65
5.4.1 Thermal Conductivity	65
5.4.2 Electrical Conductivity	66
5.4.3 Seebeck Coefficient	68
5.4.4 Power Factor	71
5.4.5 Figure-of-merit	72
5.5 Conclusion	73
6. Conclusion	74
References	76

List of Figures

Figure 1: Illustration of the Seebeck effect ⁶	2
Figure 2: Illustration of the Peltier effect ⁶	3
Figure 3: A typical thermoelectric module ³	4
Figure 4: ZT as a function of charge carrier concentration ¹²	9
Figure 5: Left: Type-I clathrate ($Pm\bar{3}An$); center: Type-III clathrate ($P4_2/mnm$); right: Type-VII clathrate ($I43m$) ³⁵	15
Figure 6: Left: Tetrakaidecahedral shaped cage; Right: Dodecahedral shaped cage ³⁵	16
Figure 7: Type I clathrate unit cell ³⁸	17
Figure 8: Ar filled glove box	21
Figure 9: Vacuum Line.....	22
Figure 10: Programmable furnaces (bottom) and manual furnaces (top)	23
Figure 11: INEL XRG 3000 Powder X-ray Diffractometer	24
Figure 12: Single crystal apparatus at the University of Waterloo	25
Figure 13: LEO 1530 FESEM equipped with an EDX Pegasus 1200.....	27
Figure 14: Characteristic X-ray photon generation possibilities in EPMA ⁵⁹	28
Figure 15: JEOL JXA-8200 electron microprobe ⁶⁰	29
Figure 16: FR-210-30T hot press by Oxy-Gon Industries	30
Figure 17: Thermal diffusivity measurement instrument.....	31
Figure 18: ULVAC ZEM-3	32
Figure 19: Sample placement in ULVAC ZEM-3 machine.....	32
Figure 20: XRD pattern for sample with $x = 0.1$ before and after hot pressing and being compared to calculated sample with $x = 0$	35
Figure 21: XRD pattern of sample with $x = 0.2$ before and after hot pressing and being compared to calculated sample with $x = 0$	36
Figure 22: Clockwise from top left mapping of: Ba, La, Ge, Ga	37
Figure 23: SEM image of the sample with $x = 0.1$ with atomic percent determined at different spots	38
Figure 24: Clockwise from top left mapping of: Ba, La, Ge, Ga	39
Figure 25: SEM image of the sample with $x = 0.2$	40
Figure 26: Thermal conductivity for La samples	43
Figure 27: Electrical conductivity of La samples	44
Figure 28: Seebeck coefficient of La clathrates	46
Figure 29: Lorenz numbers of La samples.....	47
Figure 30: Lattice thermal conductivity for La samples.....	48
Figure 31: Power factor of La clathrates.....	49
Figure 32: Figure-of-merit for La samples.....	50
Figure 33: Solubility limit for Eu containing clathrates.....	52
Figure 34: XRD results for Eu containing clathrates before hot pressing	53
Figure 35: XRD analysis for Eu clathrates after all measurements	54
Figure 36: EDX mapping of the sample with $x = 0$. Clockwise from top left: Ba, Ga and Ge	58

Figure 37: SEM image for the sample with $x = 0$ with atomic percentage at various spots	59
Figure 38: SEM image for the sample with $x = 0.1$	60
Figure 39: SEM image for the sample with $x = 0.2$	61
Figure 40: SEM image for the sample with $x = 0.3$	62
Figure 41: Thermal Conductivity results for Eu containing clathrates.....	65
Figure 42: Electrical conductivity of Eu containing clathrates.....	67
Figure 43: Seebeck coefficient for Eu containing clathrates.....	68
Figure 44: Lorenz number for Eu containing clathrates	69
Figure 45: Lattice thermal conductivity for Eu containing clathrates.....	70
Figure 46: Power Factor for Eu containing clathrates	71
Figure 47: Figure-of-merit for Eu containing clathrates	72

List of Tables

Table 1: Selected filled skutterudites with high ZT	12
Table 2: Cages involved in the formation of clathrates ³⁵	14
Table 3: Summary of ZT for Type-I clathrates.....	20
Table 4: Atomic percent for the sample with $x = 0.1$ sample at various spots as measured by EDX	38
Table 5: Atomic percent for the sample with $x = 0.2$ measured by EDX	40
Table 6: Atomic composition (in %) for the sample with $x = 0.1$ as measured by EPMA	41
Table 7: Atomic composition (in %) for the sample with $x = 0.2$ as measured by EPMA	42
Table 8: Crystallographic details of $Ba_{8-x}Eu_xGa_{16}Ge_{30}$ with Eu placed on both $2a$ and $6d$ Wyckoff positions.....	55
Table 9: Crystallographic details of $Ba_{8-x}Eu_xGa_{16}Ge_{30}$ with $2a$ position occupancy fixed at 0	56
Table 10: EDX Spot analysis for the sample with $x = 0$	59
Table 11: EDX Spot analysis for the sample with $x = 0.1$	60
Table 12: EDX Spot analysis for the sample with $x = 0.2$	61
Table 13: EDX Spot analysis for the sample with $x = 0.3$	62
Table 14: EPMA analysis for the sample with $x = 0$	63
Table 15: EPMA analysis for the sample with $x = 0.2$	63
Table 16: EPMA analysis for the sample with $x = 0.5$	64

Glossary

ZT	Figure-of-merit
TE	Thermoelectric
S	Seebeck coefficient
σ	Electrical conductivity
κ	Thermal conductivity
XRD	X-ray diffraction
PXRD	Powder X-ray diffraction
SXRD	Single Crystal X-ray diffraction
PGEC	Phonon Glass Electron Crystal
Ln	Lanthanide
BGG	$Ba_8Ga_{16}Ge_{30}$
est.	estimated
Lit.	Literature
SPS	Spark Plasma Sintering
RTG	Radioisotope Thermoelectric Generators

1. Introduction

Energy is currently a burning issue facing the world today. Continuously increasing energy demands with a concern for the environment have led to a recent push for greener technologies. Energy loss is also a big problem as a lot of energy produced through traditional power generation methods such as based on fossil fuels is lost as waste heat.¹ This is where thermoelectric (TE) materials have their use. These materials are the only materials known to convert waste heat into useful electricity.² TE materials are environmentally clean, noise free and contain no mechanical moving parts.³ These materials have a wide range of possible applications including increasing fuel efficiency for automobiles by harvesting their waste heat as well as converting waste heat into useful energy for locomotives, manufacturing plants and other areas. TE materials can also be used in refrigeration applications using Peltier coolers and these refrigerators are much more environmentally friendly than conventional refrigeration techniques as they do not emit any greenhouse gases into the atmosphere.⁴ Significant fossil fuel savings and green house emission reductions make TE materials quite desirable.

1.1 Thermoelectric Effects History

In 1821, German physicist, Thomas Johann Seebeck, discovered that when two different conductors were connected in a closed loop one junction was heated; a nearby compass needle would be deflected.⁵ In his honour, this effect would later be called the Seebeck effect. An illustration of the Seebeck effect is presented in Figure 1. When one end of a thermoelectric material is heated while the other end is kept at a cooler temperature, charge carriers diffuse from

the hotter side towards the colder side thus creating an electrical current. Electrons are the charge carriers in *n*-type semiconductors, whereas holes are the charge carriers in *p*-type semiconductors.

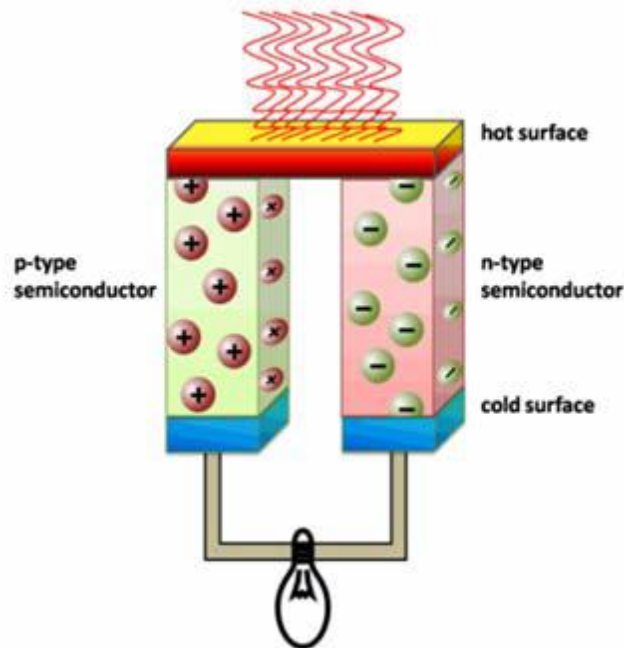


Figure 1: Illustration of the Seebeck effect⁶

A few years after Seebeck's discovery, the French physicist, Jean Charles Athanase Peltier, discovered that when a current is passed through two different conductors, a temperature change was observed at their junction.⁵ This would later be called the Peltier effect in his honour. The Peltier effect is demonstrated in Figure 2.

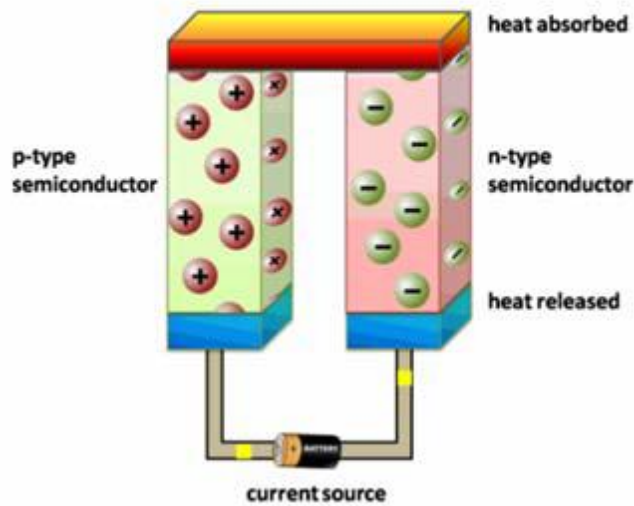


Figure 2: Illustration of the Peltier effect⁶

Finally in 1851, William Thomson, also known as Lord Kelvin, established a relationship between the Seebeck and Peltier effects and showed experimentally the heating or cooling of a current-carrying material with a temperature gradient.⁵ This is called the Thomson effect. Together these three effects define the thermoelectric phenomena in materials.

1.2 Thermoelectric Applications

Thermoelectric materials have been used in various ways, from space and military applications to day-to-day use. A typical thermoelectric generator is shown in Figure 3. This module consists of *p*-type and *n*-type legs, which are connected by metallic shunts usually made of a metallic conductor such as Cu. The metallic shunts are covered by ceramic plates. The temperature difference along the module causes charge carriers to diffuse from the hot side to the cold side which causes a buildup of charges on one end creating an electrostatic potential. The

charge carriers would start to flow within to device to maintain equilibrium. Maintaining a temperature difference would cause current to flow.

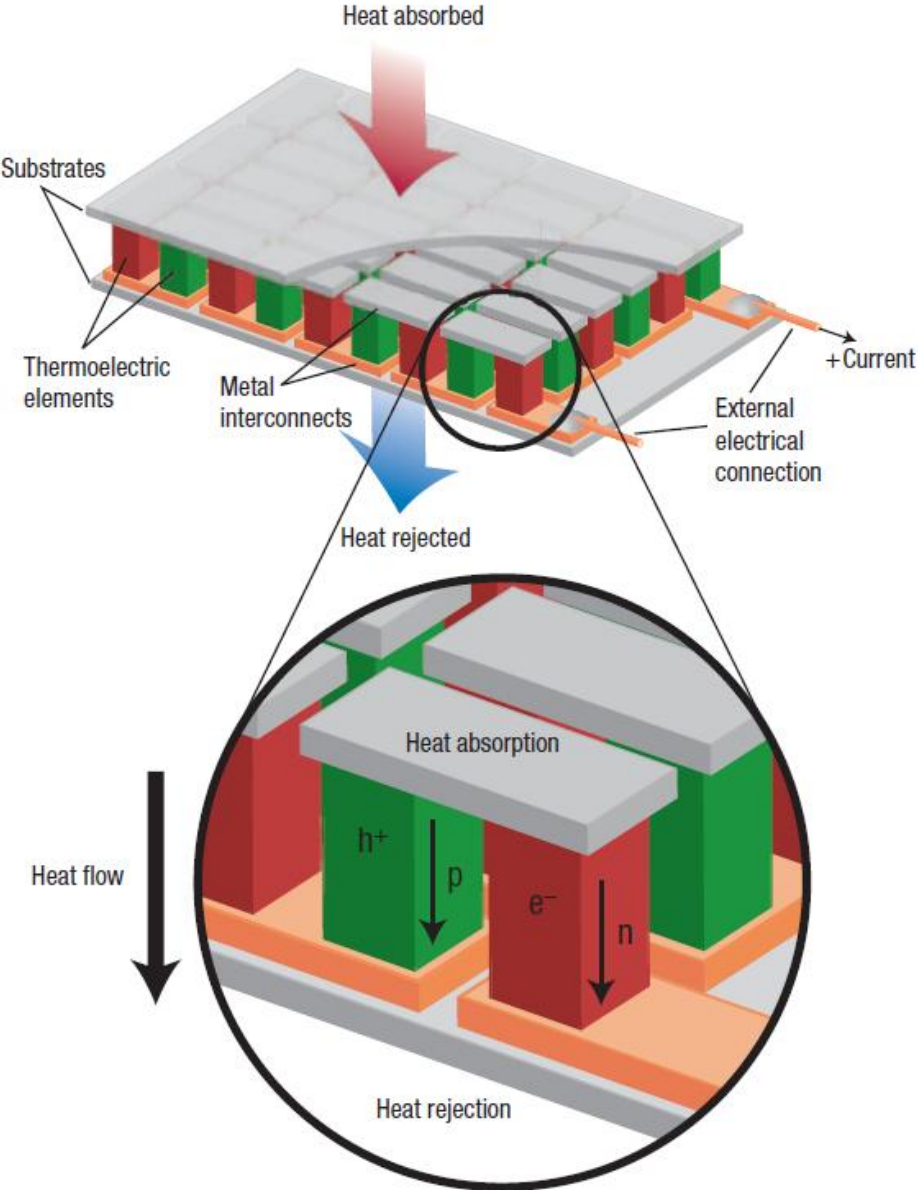


Figure 3: A typical thermoelectric module³

1.3 Thermoelectric figure-of-merit

Potential thermoelectric materials can be evaluated quickly using the dimensionless thermoelectric figure-of-merit. The formula for the figure-of-merit is given in equation 1.1.⁷

$$ZT = \frac{S^2 \sigma}{\kappa} T \quad (1.1)$$

In the formula above, S is the Seebeck coefficient, σ is the electrical conductivity, κ is the thermal conductivity and T is the temperature. Materials with high ZT are considered good for thermoelectric applications. From the formula above, it is clear that in order to be a good thermoelectric material; the material must possess a high electrical conductivity and Seebeck coefficient while maintaining low thermal conductivity. The figure-of-merit is related to the Carnot efficiency via equation 1.2.⁶

$$\eta = \frac{T_H - T_C}{T_H} \cdot \frac{\sqrt{1 + ZT} - 1}{\sqrt{1 + ZT} + T_C/T_H} \quad (1.2)$$

In equation 1.2, T_C is the temperature of the cold side and T_H is the temperature of the hot side. Using this equation, researchers can figure out the efficiency of thermoelectric devices based on how much energy was input through heat and how much energy was output by the thermoelectric material. This equation can be utilized to compare the efficiency of thermoelectric devices with other technologies. For instance, standard combustion engines have an efficiency of 33%, while current thermoelectric devices have efficiencies around 2-14%.^{6,8} From formula 1.2, it can be seen that with a ZT of around 1 and temperature of the cold side of 300 K and the hot side temperature of around 600 K, an efficiency of 10% can be achieved.⁹ It is clear that researchers need to improve the ZT of materials considerably. Each term in the ZT equation will be looked at in detail starting with the Seebeck coefficient.

1.4 Seebeck Coefficient

The Seebeck coefficient has the units of $V K^{-1}$ but most often units of $\mu V K^{-1}$ are used. In simple terms, the Seebeck coefficient is the ratio of the potential difference, ΔV , obtained when a material is subjected to a temperature gradient, ΔT . Mathematically speaking, $S = \frac{\Delta V}{\Delta T}$. The Seebeck coefficient is negative for n -type and positive for p -type materials. In degenerate semiconductors and metals, the Seebeck coefficient depends on the temperature as described in equation 1.3.³

$$S = \frac{8\pi^2 k^2}{3eh^2} m^* T \left(\frac{\pi}{3n}\right)^{2/3} \quad (1.3)$$

In equation 1.3, k is Boltzmann's constant, h is Planck's constant and e is the charge of the electron which is also a constant. Then, the Seebeck coefficient is proportional to the effective mass of charge carriers, m^* . Also, a small charge carrier concentration, n , is needed for a large Seebeck coefficient.

1.5 Electrical Conductivity

The electrical conductivity is the ability of the material to move charge carriers through the material. The formulae associated with electrical conductivity are presented in equations 1.4 and 1.5:

$$\sigma = n\mu e \quad (1.4)$$

$$\mu = \frac{e\tau}{m^*} \quad (1.5)$$

The electrical conductivity, σ , is proportional to the charge carrier concentration, n , as well as the mobility of the charge carriers, μ . Mobility, in turn, is proportional to the relaxation time, τ , which is the time between collisions of charge carriers, and inversely proportional to m^* . Thus, factors that enhance the Seebeck coefficient, namely low carrier concentration and high effective mass, are factors that cause a lower electrical conductivity.

1.6 Thermal Conductivity

The thermal conductivity describes the materials ability to conduct heat through the material. There are two components to thermal conductivity which can be seen in formula 1.6:

$$\kappa_{tot} = \kappa_e + \kappa_l \quad (1.6)$$

The total thermal conductivity consists of the electronic component of thermal conductivity, κ_e , which describes heat carried by the charge carriers and the lattice component of thermal conductivity, κ_l , which describes heat transferred through lattice vibrations (phonons). Wiedemann-Franz law describes the electronic contribution of thermal conductivity in metals and narrow band gap semiconductor. The law states that the thermal conductivity is related to electrical conductivity via the relationship described in 1.7:³

$$\kappa_e = L\sigma T \quad (1.7)$$

It can be seen that the electronic component of thermal conductivity is directly proportional to electrical conductivity. In the equation 1.7, L is the Lorenz number which can be determined through the use of following equations assuming a single parabolic band model.¹⁰

$$F_j(\eta) = \int_0^\infty \frac{x^j}{1+e^{x-\eta}} dx \quad (1.8)$$

$$S = \frac{k_B}{e} \left\{ \frac{(2+\lambda)F_{1+\lambda}(\eta)}{(1+\lambda)F_\lambda(\eta)} - \eta \right\} \quad (1.9)$$

$$L = \left(\frac{k_B}{e} \right)^2 \left\{ \frac{(1+\lambda)(3+\lambda)F_\lambda(\eta)F_{2+\lambda}(\eta) - (2+\lambda)^2 F_{1+\lambda}^2(\eta)}{(1+\lambda)^2 F_\lambda^2(\eta)} \right\} \quad (1.10)$$

$F_j(\eta)$ is a Fermi integral of order j .¹⁰ From the measured Seebeck coefficient, S , the reduced Fermi energy, η , can be determined. When acoustic phonon scattering is the dominant scattering mechanism, $\lambda = 0$.¹¹ Finally, Lorenz number can be determined from equation 1.10.¹¹ Once the Lorenz numbers and electrical conductivity values are known, the electronic component of the thermal conductivity can be calculated. The lattice component of the thermal conductivity can thereafter be easily determined by subtracting the electronic component from the total measured thermal conductivity.

1.7 Material Selection

Materials with a high figure-of-merit display good thermoelectric properties. From the ZT equation, it is evident that a material which displays high Seebeck coefficient, high electrical conductivity and low thermal conductivity is suited to thermoelectric applications. Figure 4 illustrates different materials and their relationship to ZT .

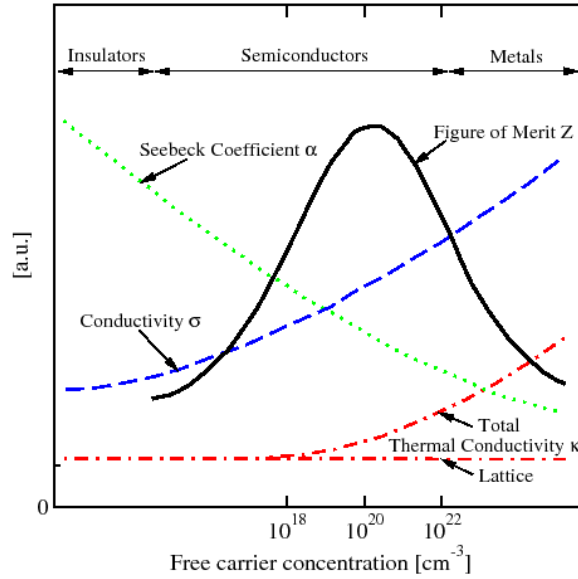


Figure 4: ZT as a function of charge carrier concentration¹²

Figure 4 shows that metals have good electrical conductivity but low Seebeck coefficient due to high carrier concentration. Furthermore, metals also have high thermal conductivity; therefore metals are not good thermoelectric materials. Insulators, on the other hand, have very low thermal conductivity and high Seebeck coefficient but are poor electrical conductors. Hence, insulators cannot be used for thermoelectric applications either. Semiconductors however, are ideal thermoelectric materials.

2. Literature Review

2.1 Bi₂Te₃

Bi₂Te₃ is the most common commercially used room temperature thermoelectric material. It can be turned into either *p*-type or *n*-type material depending on which type of dopants are introduced.⁵ This material is used in thermoelectric coolers which take advantage of the Peltier effect. Bi₂Te₃ has also been used in space probes which utilize RTGs (Radioisotope Thermoelectric Generators).¹³ In an RTG, high energy radioactive fuel is used to generate heat. The fuel for the heat source is Plutonium-238 in the form of PuO₂. Alpha particles are released in the decay process of ²³⁸Pu. These particles bombard the container housing the radioactive material which converts the energy released into heat which is ultimately the source of heat for the thermoelectric generators.¹³

Much work has been done on Bi₂Te₃. Caillat *et al.* started working on this material in the 1950s to improve its thermoelectric properties.⁶ Other work done on this material includes mixing it with Bi₂Se₃ or Sb₂Te₃.⁵ Nanostructuring as well as making Bi₂Te₃ nanotubes have also been performed.¹⁴ Solid solutions have also been investigated for this material e.g. (Sb,Bi)₂Te₃ or Bi₂(Se,Te)₃.⁵ A layered nanostructure *p*-type Bi₂Te₃ achieved a maximum *ZT* of 1.35 at 300 K.¹⁵

PbTe is also a good performing thermoelectric material. It has also been used since the 1960's mainly by NASA for its space missions. Similar to Bi₂Te₃, PbTe is used in RTG on spacecrafts. The Mars rover Curiosity uses PbTe based alloys. Historically, PbTe had a *ZT* of ~ 0.8.¹⁶ The thermoelectric performance of PbTe has improved significantly since then. *p*-type PbTe materials with high Na doping have shown high *ZT* of ~ 1.4 at ~750 K.¹⁷ In other work,

$\text{PbTe}_{1-x}\text{I}_x$ displayed a ZT of around 1.4 between 700-850 K.¹⁸ The best result for PbTe was achieved when p -type PbTe was nanostructured with SrTe, which had ZT value of ~ 2.2 at 915 K.¹⁹

Thallium telluride is another class of thermoelectric materials. These materials have low thermal conductivity, almost one third that of Bi_2Te_3 .²⁰ Sharp *et al.* reported that Tl_2SnTe_5 exhibited a ZT of 0.85 at 400 K.²¹ Wölfing *et al.* showed that Tl_9BiTe_6 has a ZT of 1.2 at 500 K.²² Other high ZT materials include $\text{Tl}_{8.05}\text{Sn}_{1.95}\text{Te}_6$ with a ZT of 1.26 at ~ 700 K and $\text{Tl}_{8.10}\text{Pb}_{1.90}\text{Te}_6$ with a ZT of 1.46 at ~ 700 K.²³

2.2 PGEC Concept

Although thermoelectric phenomena were discovered in the early 19th century, the thermoelectric field remained relatively dormant because of low efficiency of thermoelectric materials. The field experienced considerable interest when Slack proposed his PGEC (phonon-glass-electron-crystal) concept.²⁴ In the PGEC concept, it was postulated that an ideal thermoelectric material should behave like a glass when it comes to thermal conductivity and like an electron single crystal when it comes to electrical conductivity.²⁴

Another similar concept is the PLEC (Phonon Liquid Electron Crystal) concept. Work has been done on Cu_{2-x}S which follows this concept. The copper ions in this material have liquid-like mobility. This leads to very strong phonon scattering, which leads to very low thermal conductivity. For Cu_2S , a ZT of 1.7 was achieved at 1000 K.²⁵ Work has also been on a similar compound Cu_{2-x}Se . This compound had a ZT of 1.5 at 1000 K for the sample with $x = 0$.²⁶ The problem with these materials, however, is the degradation caused by the high mobility of copper ions.²⁷ To counter this problem, $\text{BaCu}_{5.9}\text{SeTe}_6$ was synthesized. The addition of

heavier atoms such as Ba and Te is likely to reduce the copper ion mobility. This material reached a ZT of 0.8 at 600 K.²⁸

2.3 Skutterudites

Skutterudites are one of the materials that are often viewed as PGEC materials. Skutterudites have the general formula TPn_3 where $T = Co, Rh, \text{ or } Ir$ and Pn is an element from the pnictogen group usually $P, As \text{ or } Sb$.¹ Skutterudites are being considered for use in automobiles to recover waste heat and improve fuel efficiency.²⁹ Skutterudites crystallize in a cubic space group similar to Type-I clathrates. The space group for skutterudite is $Im\bar{3}$ and the structure is of $CoAs_3$ -type.¹ This structure contains two large intrinsic holes per unit cell. These holes can be filled with guest atoms similar to Type-I clathrates. This rattling motion of the guest atoms would lead to a reduction in thermal conductivity. Filled skutterudites have shown good thermoelectric properties. Table 1 below lists several filled skutterudites with high ZT .

Table 1: Selected filled skutterudites with high ZT

Material	Maximum ZT	Temperature (K)
$Yb_{0.19}Co_4Sb_{12}$ ³⁰	1.14	640
$Ca_{0.18}Co_{3.97}Ni_{0.03}Sb_{12.4}$ ³¹	0.99	800
$Ba_{0.13}In_{0.14}Co_4Sb_{11.75}$ ³²	1.19	850
$Ba_{0.24}Co_4Sb_{12}$ ³³	1.10	850

2.4 Clathrates

Clathrates form cage structures with guest atoms possibly trapped inside the cages formed by host atoms. Clathrates were first discovered by Sir Humphry Davy in the early 19th century.³⁴ The clathrates discovered by Davy included gas molecules such as methane, carbon



dioxide, ethane, propane, and other gases trapped inside cages where water acted as the host molecules. Since the PGEC concept was proposed by Slack, many different semiconducting clathrates have been discovered including Type I-IX and Type H.³⁵ Most clathrates have guest atoms occupying cages formed by host atoms. The difference between these types of clathrates is the nature, size and the number of the cages that make up the clathrates. For thermoelectric purposes, Type I, Type III and Type VIII clathrates have been identified as potential materials.³⁶⁻
³⁸ Interestingly, $\text{Ba}_8\text{Ga}_{16}\text{Sn}_{30}$ and $\text{Eu}_8\text{Ga}_{16}\text{Ge}_{30}$ have two modifications: the α phase, which is a Type VIII clathrate, and the β phase which is a Type I clathrate.^{39,40} For Type III clathrates, a figure-of-merit of 1.25 was achieved for $\text{Ba}_{24}\text{Ga}_x\text{Ge}_{100-x}$ on a sample with $x = 15$.³⁷

2.4.1 Clathrate Types

Many different clathrate types are theoretically possible. Eleven clathrate types have been discovered so far. This includes Type-I to Type-IX as well as Type-H and Type-II-4H. Each clathrate structure contains host atoms which make up the cages and guest atoms which are enclosed in cages surrounded by host atoms. The main difference between all types of clathrates is the nature of cages contained within them. There are numerous building block cages which make up the clathrates. The combination of the different building blocks determines the type of clathrate. The building blocks are formed by polyhedra which are detailed in Table 2.

Table 2: Cages involved in the formation of clathrates³⁵

Polyhedral notation	Shape	Present in Clathrate
[3 ³ 4 ³]		VIII
[4 ⁴ 5 ⁴]		VI
[5 ¹²]		I, II, III, IV, V, IX, H, II-4H
[4 ³ 5 ⁶ 6 ³]		H
[3 ³ 4 ³ 5 ⁹]		VIII
[5 ¹² 6 ²]		I, III, IV
[4 ⁶ 6 ⁸]		VII
[5 ¹² 6 ³]		III, IV
[5 ¹² 6 ⁴]		II, V, II-4H

$[4^3 5^9 6^2 7^3]$		VI
$[5^{12} 6^8]$		H

Selected clathrate types which have been shown to be thermoelectric materials are presented in the following figure.

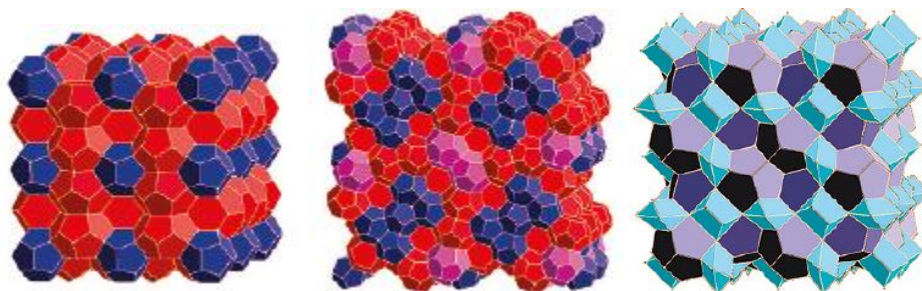


Figure 5: Left: Type-I clathrate ($Pm\bar{3}An$); center: Type-III clathrate ($P4_2/mnm$); right: Type-VII clathrate ($I\bar{4}3m$)³⁵

2.4.2 Type I clathrates

Type-I clathrates consist of two types of interlocking cages. One cage is the dodecahedron, a cage with twelve pentagonal faces and the other type of cage is called a tetrakaidecahedron which consists of two hexagonal and twelve pentagonal faces.¹ The two different types of cages are shown in Figure 6:

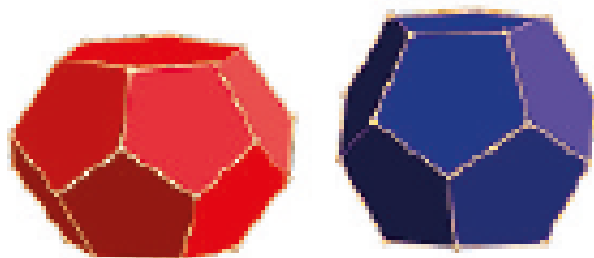


Figure 6: Left: Tetrakaidecahedral shaped cage; Right: Dodecahedral shaped cage³⁵

The cage is made up of host atoms and the guest atoms sit inside these cages. Type-I clathrates have the general formula $M_8A_{16}X_{30}$ where M is the guest atom usually from the second group of the periodic table, which can be either Ba or Sr. Other guest atoms include Eu, Na, K. A is from Group 13 and can be either Ga, In or Al, and X is usually from Group 14 which includes Si, Sn or Ge. Other host atoms have also been tried including Ni, Zn, Cu and other atoms. The most common material investigated so far is $Ba_8Ga_{16}Ge_{30}$. The cubic structure of Type I clathrates belongs to the $Pm\bar{3}n$ space group. The unit cell contains 46 tetrahedrally bonded host atoms and eight guest atoms. Within one unit cell, there are a total of two dodecahedral cages and six tetrakaidecahedral cages. Figure 7 shows the unit cell of this structure.

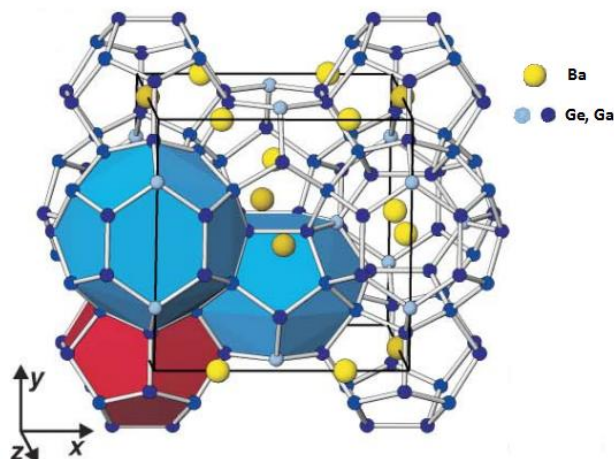


Figure 7: Type I clathrate unit cell³⁸

The Zintl concept governs the stoichiometry of the Type-I clathrate structure. Ba, or any other guest atom, donates its valence electrons to the host framework formed by Ga-Ge or other host atoms. Host atoms are bonded tetrahedrally; therefore they require four valence electrons to share with the surrounding atoms. Since there are 46 host atoms within the unit cell and each atom requires four electrons, there should be $46 \times 4 = 184$ electrons available to the host framework. Each of the 30 Ge atoms has four valence electrons thus $30 \times 4 = 120$ electrons are provided for by Ge. Ga has three valence electrons and there are a total of 16 Ga atoms in the unit cell, so $16 \times 3 = 48$ electrons are coming from Ga. The rest of the electrons are donated by Ba atoms. Each Ba atom donates two valence electrons to the host structure, thus there are $8 \times 2 = 16$ electrons from the guest. Hence, in Type-I clathrates, there total number of valence electrons within the unit cell are $120 + 48 + 16 = 184$.

Another way to look at this structure is by assigning oxidation states. Ba donates two electrons to the host framework so it has a charge of +2. Ga and Ge need four valence electrons each to form tetrahedral bonds. Ge already has four valence electrons. It neither donates nor

accepts electrons. Ga on the other hand has three valence electrons so it needs one additional electron for the needed four electrons which it accepts from the Ba atoms. Therefore Ga has a charge of -1. In total, 8 Ba atoms have a charge of 16+ and 16 Ga atoms have a charge of 16- balancing the overall charge.

2.4.3 Clathrate Literature Review

In 1998, Nolas *et al.* first reported on the Type-I clathrate $\text{Sr}_8\text{Ga}_{16}\text{Ge}_{30}$ as a potential thermoelectric material with an estimated ZT value at 700 K around 1.0.⁴¹ For the same material, Cao *et al.* showed that with partial substitution of Ga with In in $\text{Sr}_8\text{Ga}_{16}\text{Ge}_{30}$, a ZT of 0.72 was achieved at 800 K.⁴² Fujita *et al.* synthesized $\text{Sr}_8\text{Ga}_x\text{Ge}_{46-x}$ with the highest ZT of 0.62 at 800 K for a sample with $x = 16.5$.⁴³ Many $\text{Ba}_8\text{Ga}_{16}\text{Ge}_{30}$ materials have been synthesized. Kuznetsov *et al.* estimated ZT of $\text{Ba}_8\text{Ga}_{16}\text{Ge}_{30}$ to be 0.7 at 700 K and $ZT = 0.87$ for $\text{Ba}_8\text{Ga}_{16}\text{Si}_{30}$ at 870 K.⁴⁴ Palmqvist *et al.* measured a ZT of 0.65 at around 900 K for $\text{Ba}_8\text{Ga}_{16}\text{Ge}_{30}$.⁴⁵ Okamoto *et al.* showed that with partial substitution of Ga with In in $\text{Ba}_8\text{Ga}_{16}\text{Ge}_{30}$, $ZT = 1.03$ was achieved at 943 K.⁴⁶ This group also tried adding TiO_2 nano-inclusions to the clathrate structure, reaching a maximum ZT of 0.7 at 770 K.⁴⁷ Anno *et al.* showed that it is possible to synthesize $\text{Ba}_8\text{Ga}_x\text{Ge}_{46-x}$ with x ranging from 12 to 20. It was noted that samples with $x = 12$ to 16, the clathrate was n -type while for samples with $x = 17$ to 20, the material was p -type. ZT around 1 was estimated for the sample $x = 18$ sample at 900 K.⁴⁸ Toberer *et al.* measured a maximum ZT of 0.8 at 1050 K for $\text{Ba}_8\text{Ga}_{16}\text{Ge}_{30}$.⁴⁹

In research focusing on the host elements, Deng *et al.* tried substitution of Ge with Al and achieved a ZT of 0.61 at 760 K for $\text{Ba}_8\text{Ga}_{16}\text{Al}_3\text{Ge}_{27}$.⁵⁰ Shi *et al.* used the transition metals Ni and Zn in the clathrates, which led to a ZT of 1.2 at 1000 K for $\text{Ba}_8\text{Ni}_{0.31}\text{Zn}_{0.52}\text{Ga}_{13.06}\text{Ge}_{32.2}$ with a polycrystalline sample.⁵¹

For single crystal clathrates, Hou *et al.* used the Czochralski pulling method to obtain single crystal $\text{Ba}_8\text{Ga}_{16}\text{Ge}_{30}$. The highest ZT value measured by this was 0.93 at 850 K with an extrapolated ZT of 1.3 at 1000 K.⁵² However, the best results for Type-I clathrate so far has been achieved by Saramat *et al.* who have used the Czochralski pulling method to grow a single crystal of $\text{Ba}_8\text{Ga}_{16}\text{Ge}_{30}$. This crystal exhibits a measured ZT of 1.35 at 900 K, and an extrapolated ZT of 1.63 at 1100 K.⁵³

As far as guest atoms are concerned, Cohn *et al.* noticed that the thermal conductivity of $\text{Eu}_8\text{Ga}_{16}\text{Ge}_{30}$ compound is lower than that of $\text{Sr}_8\text{Ga}_{16}\text{Ge}_{30}$. Eu and Sr both have an oxidation state of +2, with Eu being the heavier element. The trend is that the heavier the element is, the lower the thermal conductivity due to enhanced phonon scattering.⁵⁴

The main interest for this thesis is double filling atoms in cages of the clathrates. Here, double filling does not refer to filling one cage with two atoms, but it means having cages being occupied by different atoms. Literature on filling the cages with different atoms has been limited. Cohn *et al.*, mentioned earlier, have also shown in the same paper that the thermal conductivity of double filled $\text{Eu}_4\text{Sr}_4\text{Ga}_{16}\text{Ge}_{30}$ is lower than that of $\text{Eu}_8\text{Ga}_{16}\text{Ge}_{30}$ which indicates that double filling the cages with two different types of atoms leads to increased phonon scattering.⁵⁴ The most relevant case on double filling of the cages has been reported by Tang *et al.* This group incorporated Yb along with Ba into the cages and a maximum ZT of 1.09 at 950K was measured.⁵⁵ However, other studies have cast a doubt on the successful incorporation of Yb into the clathrate structure.⁵⁶ The Table 3 summarizes ZT for Type-I clathrates.

Table 3: Summary of ZT for Type-I clathrates

Clathrate	Maximum ZT	Temperature (K)
$\text{Ba}_8\text{Cu}_6\text{Si}_{40}$ ⁵⁷	0.28	873
$\text{Sr}_8\text{Ga}_{16.5}\text{Ge}_{29.5}$ ⁴³	0.62	800
$\text{Sr}_8\text{Ga}_{15.5}\text{In}_{0.5}\text{Ge}_{30}$ ⁴²	0.72	800
$\text{Ba}_8\text{Ga}_{16}\text{Si}_{30}$ ⁴⁴	0.87 (est.)	870
$\text{Ba}_8\text{Ga}_{16}\text{Ge}_{30}$ ⁴⁴	0.70 (est.)	700
$\text{Ba}_8\text{Ga}_{16}\text{Ge}_{30}$ 0.4 vol% TiO_2 ⁴⁷	0.70	770
$\text{Ba}_8\text{Ga}_{16}\text{Ge}_{30}$ ⁴⁵	0.65	900
$\text{Ba}_8\text{Ga}_{10}\text{In}_6\text{Ge}_{30}$ ⁴⁶	1.03	1000
$\text{Ba}_8\text{Ga}_{16}\text{Al}_3\text{Ge}_{27}$ ⁵⁸	0.61	760
$\text{Ba}_8\text{Ni}_{0.31}\text{Zn}_{0.52}\text{Ga}_{13.06}\text{Ge}_{32.2}$ ⁵¹	1.20	1000
$\text{Ba}_8\text{Ga}_{16}\text{Ge}_{30}$ ⁵²	0.93	850
$\text{Ba}_8\text{Ga}_{16}\text{Ge}_{30}$ ⁵³	1.35	900
$\text{Ba}_{7.5}\text{Yb}_{0.5}\text{Ga}_{16}\text{Ge}_{30}$ ⁵⁵	1.09	950

3. Sample Preparation and Analysis

3.1 Synthesis

All samples were synthesized from their starting elements stored in an argon-filled glove box shown in Figure 8.



Figure 8: Ar filled glove box

These were the starting elements used:

- Ba pieces, Strem Chemicals, 99.7%,
- La chips, Strem Chemicals, 99.6%
- Eu ingot, Alfa Aesar, 99.9%;
- Ga metal, Strem Chemicals, 99.99%
- Ge pieces, Alfa Aesar, 99.9999+%, metal basis

The surface of the Ba pieces, La chips and Eu ingots were covered in black layers which were thoroughly scratched off and the resultant shiny pieces were used in the reactions. Except Ba, stoichiometric amounts of all elements were used. It has been reported in literature that

starting with excess Ba gives phase pure samples therefore 25% excess Ba was used.⁵² Because of high reactivity of Ba with silica tubes, starting elements were placed inside graphite crucibles which were subsequently loaded in silica tubes. The silica tubes were placed on vacuum lines and evacuated up to $\sim 10^{-3}$ mbar shown in Figure 9.



Figure 9: Vacuum Line

An H_2/O_2 flame was used to vacuum seal the silica tubes and the tubes were placed in a programmable resistance furnace for heat treatment. The furnace was programmed to reach 973 K within 24 h, stayed at that temperature for 6 hours, increased to 1273 K over 6 h and kept there for 24 h. The temperature was then decreased to 923 K over 24 h and kept there for 144 h for annealing. Afterwards, samples were cooled to room temperature over 24 h. The resulting ingots were ground and annealed at 923 K for a further 168 h to achieve homogeneous samples.

Programmable furnaces shown at the bottom of Figure 10 were used for initial synthesis while manual furnaces shown at the top of Figure 10 were used for annealing.



Figure 10: Programmable furnaces (bottom) and manual furnaces (top)

3.2 Powder X-ray Diffraction (PXRD)

PXRD was used for analysis after completion of the synthesis. The sample has to be crushed into fine powder. INEL XRG-3000 powder diffractometer, which can collect patterns from 0 to 120°, is used to obtain powder patterns. The source used is Cu $K\alpha_1$ which has a wavelength of 1.5406 Å. X-ray diffraction is governed by Bragg's Law, which is stated in the equation (3.1):

$$n\lambda = 2d\sin\theta \quad (3.1)$$

In the equation above, θ is the angle of incidence of X-rays, d is the distance between successive atomic planes in a crystal and λ is the wavelength of the X-rays. Diffracted X-rays will either interfere constructively at certain angles or cancel out because of destructive interference at all other angles. The intensities of constructively interfering X-ray reflections are measured at all angles and a plot of intensity vs. angle is generated. The powder pattern obtained from the clathrates sample are then compared to references from literature using software such as MATCH and WPA to determine the purity of the sample by comparing it with reference powder patterns. Addition of the lanthanides does not drastically change the crystal structure or the unit cell parameter so the powder patterns will be similar to $\text{Ba}_8\text{Ga}_{16}\text{Ge}_{30}$. The diffractometer used is shown in Figure 11.



Figure 11: INEL XRG 3000 Powder X-ray Diffractometer

3.3 Single Crystal

Single crystal analysis was done using the Bruker single crystal instrument at the University of Waterloo. The X-ray source used was Mo-K_α radiation which has a wavelength of 0.71073 \AA . Single crystals (around $20\text{-}400\mu\text{m}$) were analyzed. The crystal was scanned over a period of 6

hours to collect reflections. The detector used was the Bruker Smart APEX CCD detector. The Single crystal measurement setup is shown in Figure 12.

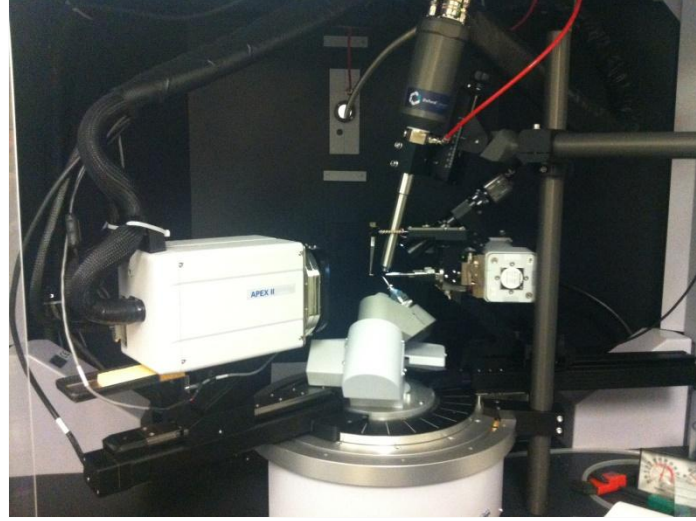


Figure 12: Single crystal apparatus at the University of Waterloo

The reflections which are observed are in reciprocal space. The scattering of the crystal is described by the scattering factor, F_{hkl} , which is the addition of the atomic scattering factor, f , of each atom in the crystal, j , and the atoms relationship to Miller indices (hkl) and atomic position (xyz). The scattering factor is presented in the equation below:

$$F_{hkl} = \sum f_j e^{2\pi i(hx_j + ky_j + lz_j)} \quad (3.2)$$

The square of the structure factor is proportional to the measured intensity of reflections, I_{hkl} , as follows: $I_{hkl} \propto |F_{hkl}|^2$. Another important property is the electron density which is related to the structure factor via the following equation:

$$\rho_{xyz} = \frac{1}{V} \sum_h \sum_k \sum_l F_{hkl} e^{-2\pi i(hx + ky + lz)} \quad (3.3)$$

From equation 3.3, if the structure factor is known, electron density in the crystal can be calculated and thus the exact location of the atomic positions within the structure can be determined. From the collected data, only the magnitude of scattering factor is known. The phase (ϕ) must also be determined as shown in the equation below.

$$F_{hkl} = |F_{hkl}|e^{i\phi} \quad (3.4)$$

The SHELXT solution software was used to refine atomic positions, occupancies and atomic displacement parameters until the difference between the observed structure factor, F_o , and calculated structure factor, F_c , is small. There are two ways of looking at this difference, R_1 , which is known as the residual factor, and wR_2 , which is known as the weighted residual factor.

$$R_1 = \frac{\sum ||F_o - F_c||}{\sum |F_o|} \quad (3.5)$$

$$wR_2 = \sqrt{\frac{\sum w(F_o^2 - F_c^2)^2}{\sum F_o^2}} \quad (3.6)$$

In equation 3.6, w refers to the weight, which is proportional to reciprocal of square of the standard uncertainty of the intensity measurement. The refinement is generally considered acceptable when R_1 values are less than 5% and wR_2 values are less than 10%.

3.5 SEM with EDX

A Scanning Electron Microscope (SEM) can be used to obtain images of samples on a scale of few micrometers. SEM takes place under vacuum where a beam of high energy electrons is fired upon the sample. The electrons beam causes outer electrons of the atoms to be scattered and those electrons are detected resulting in an image. Energy Dispersive X-ray Analysis (EDX) is also performed in conjunction with SEM which is of more interest for this

project. In EDX, the high energy electron beam ejects an electron from one of the inner shells of the atom. When the inner electron is ejected, an electron from one of the outer shells comes down to take its place and in the process releasing an X-ray photon. These are called characteristic X-rays. Each atom has its own characteristic X-ray. By detecting and analyzing the characteristic X-rays, the atomic composition can be determined.



Figure 13: LEO 1530 FESEM equipped with an EDX Pegasus 1200

3.6 EPMA

Electron Probe Microanalyzer (EPMA) is used to determine atomic composition. In EPMA, a solid sample is bombarded with an electron beam. The electron beam knocks out an inner shell electron from the atoms present in the sample. This will create an unstable vacancy which must

be filled by an electron from a higher shell. Figure 14 shows the possible outcomes when an electron from a higher shell drops down to fill a vacancy in the inner shell. When the higher shell electron comes down to take fill the vacancy, a photon is emitted. The photon is in the region of X-rays. The energy of the photon corresponds to the difference in energies of the outer and inner shell. Each atom has its own characteristic X-ray that is released via this process. These characteristic X-rays can be detected and the data can be used to determine atomic composition of the sample. EPMA is used in conjunction with SEM.

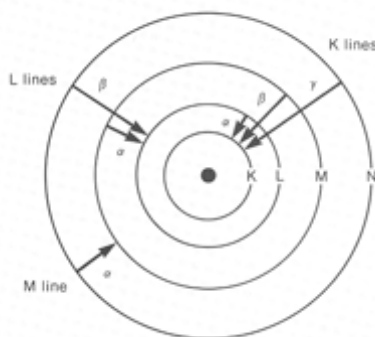


Figure 14: Characteristic X-ray photon generation possibilities in EPMA⁵⁹

Chemical microanalysis on the samples were done in was done in Geocampus Lankwitz Berlin, Germany by the JEOL JXA-8200 electron microprobe shown in Figure 15. For the measurements the samples were embedded in epoxy, ground flat and finally polished with $\frac{1}{4}$ μm diamond paste. For electron beam analysis they were carbon coated by thermal evaporation in a Leica EM SCD500 using the same laboratory methods as for the reference materials. The standards used were natural barite, BaSO_4 (Ba), synthetic LaPO_4 (La), synthetic GaAs (Ga), and elemental Ge (Ge). The samples were investigated by back scattered electron imaging before

determining spots for point analyses. Wavelength-dispersive analysis was performed by a fully focused electron beam with 15 kV acceleration voltage and 20 nA beam current.



Figure 15: JEOL JXA-8200 electron microprobe⁶⁰

3.7 Hot Press

Once the XRD analysis reveals that the sample is pure, the next step is to consolidate the powder and form pellets for physical property measurements. The idea is to obtain a pellet which has a density which is very close to the theoretical density of the clathrates. High temperature and pressure is used to weld the powder grains together resulting in a solid pellet. This resulted in pellets with a density $> 95\%$ of the theoretical density. The instrument used for hot pressing is provided by Oxy-Gon Industries shown in Figure 16.



Figure 16: FR-210-30T hot press by Oxy-Gon Industries

3.8 Thermal Conductivity Measurement

Once the pellet has been obtained from hot press, the next step would be to measure its thermal conductivity. The Flashline 3000 diffusivity system provided by TA Instruments is used to perform this measurement. This equipment does not directly measure the thermal conductivity, rather it measures thermal diffusivity. Thermal conductivity can then be subsequently obtained from the data. During the measurement the sample chamber is purged with Ar gas and a high intensity short duration energy pulse is fired by the machine on the front face of the disk shaped pellet. The temperature on the rear face of the disk is recorded using an infrared detector. The diffusivity can then be obtained using the equation 3.7:

$$\alpha = 0.1388 \frac{L^2}{t_{1/2}} \quad (3.7)$$

In equation 3.7, α is the thermal diffusivity, L is the thickness of the pellet, $t_{1/2}$ is the time it takes for the temperature on the rear face of the pellet to reach half of its original value. The thermal conductivity can then be determined using the following relation:

$$\kappa = \alpha \rho_D C_p \quad (3.8)$$

In equation 3.8, κ is the thermal conductivity, ρ_D is the density of the pellet, which is usually measured utilizing the Archimedes principle and C_p is the heat capacity of the pellet, which is obtained using the Dulong-Petit Law which can be described mathematically as follows:

$$C_p = \frac{3R}{M} \quad (3.9)$$

R in equation 3.9 is the universal gas constant and M is the averaged molecular mass of the material. The thermal diffusivity system is shown in Figure 17.



Figure 17: Thermal diffusivity measurement instrument

3.9 Seebeck Coefficient and Electrical Conductivity Measurement

Seebeck coefficient and electrical conductivity are measured simultaneously using the ZEM-3 measurement instrument acquired from ULVAC. The instrument is shown in Figure 18.



Figure 18: ULVAC ZEM-3

The pellet obtained from hot pressing is cut into rectangular bar preferably with dimensions of $10 \times 2 \times 2$ mm. A diamond saw is used to cut the rectangular bar from the pellet. The bar is placed vertically between the two electrodes as shown in Figure 19.

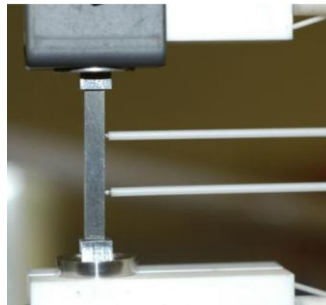


Figure 19: Sample placement in ULVAC ZEM-3 machine

The bottom of the pellet is heated to the desired measurement temperature and a constant current is passed through the bar. Thermocouples measure the temperature differences between

the two parts of the bar and the potential difference between the thermocouples is also measured thus Seebeck coefficient is measured using the following relationship.

$$S = \frac{\Delta V}{\Delta T} \quad (3.10)$$

Electrical conductivity is also measured in addition to Seebeck coefficient by the ZEM instrument. It utilizes Ohm's law shown in equation 3.11.

$$R = V/I \quad (3.11)$$

Since the constant current passed through the bar is known and the voltage between the two thermocouples is measured, the resistance, R , of the material can be obtained by the equation above. The resistivity of the bar, ρ_R , can then be determined by the following formula:

$$\rho_R = R \frac{A}{L} \quad (3.12)$$

In equation 3.12, A is the cross sectional area of the measured bar and L is the distance between the probes. The dimensions of the bar are measured using a micrometre beforehand, which are input as the sample parameters in ZEM. The electrical conductivity is simply the inverse of the resistivity.

$$\sigma = \frac{1}{\rho_R} \quad (3.13)$$

4. Lanthanum filled clathrates

4.1 Synthesis

All samples were synthesized as mentioned earlier in Section 3.1

For La samples, $\text{Ba}_{7.8}\text{La}_{0.2}\text{Ga}_{16}\text{Ge}_{30}$ and $\text{Ba}_{7.9}\text{La}_{0.1}\text{Ga}_{16}\text{Ge}_{30}$ were synthesized successfully with enough samples allow for physical property measurements. These samples will be referred to as $x = 0.1$ and $x = 0.2$ respectively.

4.2 XRD Analysis

The samples were determined to be phase-pure according to powder X-ray diffraction patterns. The diffraction patterns were obtained on an Inel powder diffractometer, which is equipped with a position-sensitive detector and utilizes $\text{Cu K}\alpha_1$ radiation. After all physical property measurements were completed, XRD analysis was performed again to ensure materials did not decompose during measurements while subjected to different heat cycles. The powder patterns are compared to reference $\text{Ba}_8\text{Ga}_{16}\text{Ge}_{30}$ sample.

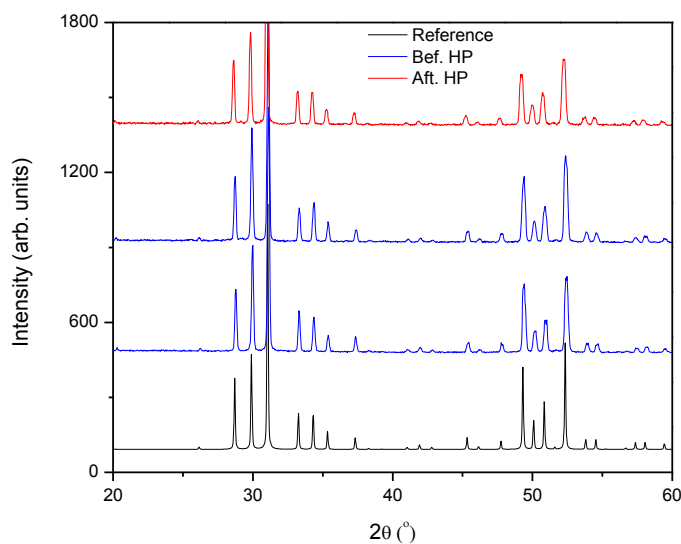


Figure 20: XRD pattern for sample with $x = 0.1$ before and after hot pressing and being compared to calculated sample with $x = 0$

Two samples with $x = 0.1$ were synthesized separately and mixed together to form the hot pressed pellet. Both samples display similar powder patterns to reference before hot pressing. After hot pressing and physical property measurements, the sample does not decompose as evident in the figure.

As was the case with sample with $x = 0.1$, two separate samples were synthesized with $x = 0.2$ as well and mixed together for the purposes of hot pressing. After measurement, sample with $x = 0.2$ also showed no signs of decomposition as presented in Figure 21.

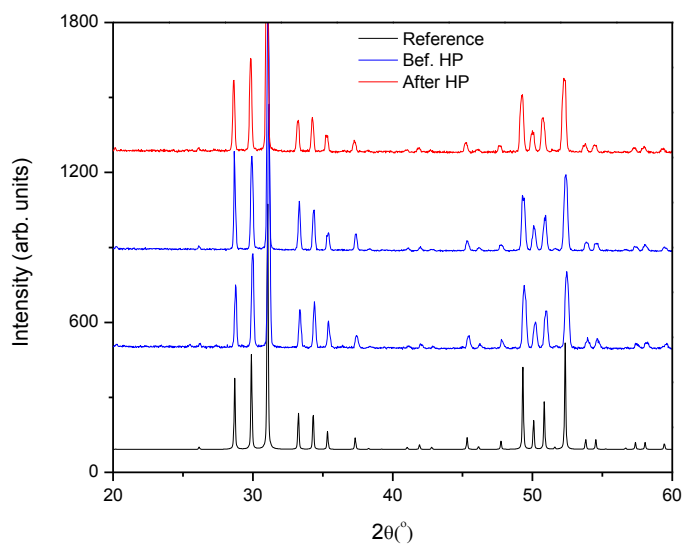


Figure 21: XRD pattern of sample with $x = 0.2$ before and after hot pressing and being compared to calculated sample with $x = 0$

All pure samples were hot-pressed into circular pellets with a 12.7 mm diameter and a thickness of ~ 2 mm under argon flow inside a graphite die using the FR-210-30T hot press from Oxy-Gon Industries. The optimized pressing conditions for all samples were 77 MPa at 1100 K with a 2 h dwell time. The densities for all samples were measured using Archimedes principle which resulted in $>96\%$ theoretical densities for all samples. Once the hot pressed pellet was obtained, physical properties were measured.

4.3 EDX Analysis

4.3.1 $x = 0.1$

Mapping of all elements was performed via EDX on the sample with $x = 0.1$ and is presented in Figure 22.

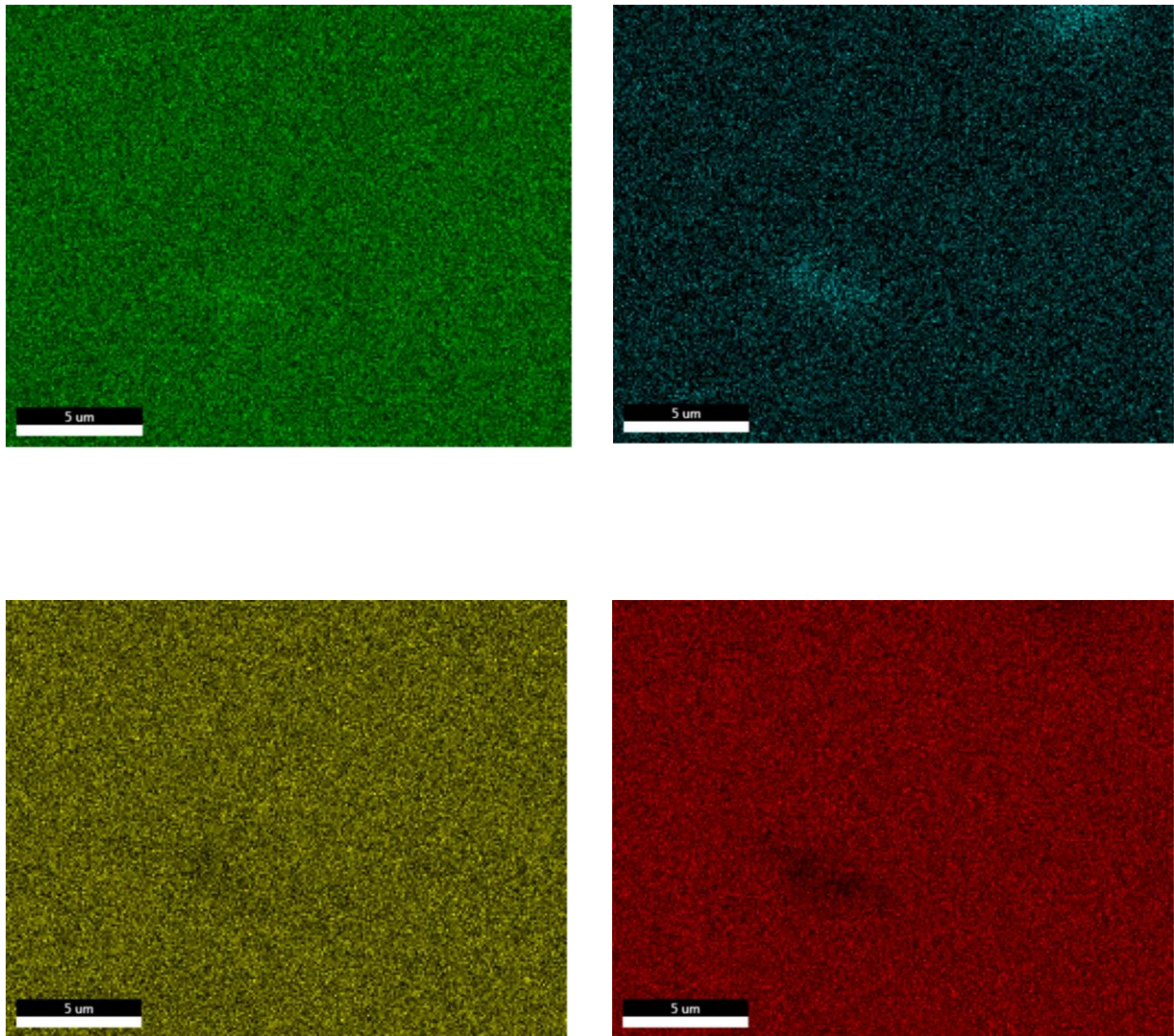


Figure 22: Clockwise from top left mapping of: Ba, La, Ge, Ga

It can be seen from the EDX mapping that all elements are present uniformly throughout the sample. However there is one spot which is Ba and La rich (just below the center in the image). La mapping also shows another bright spot with high La content in top right hand corner.

Atomic percent was also measured on the sample with $x = 0.1$ via EDX. The atomic percent was measured at different spots as seen in Figure 23.

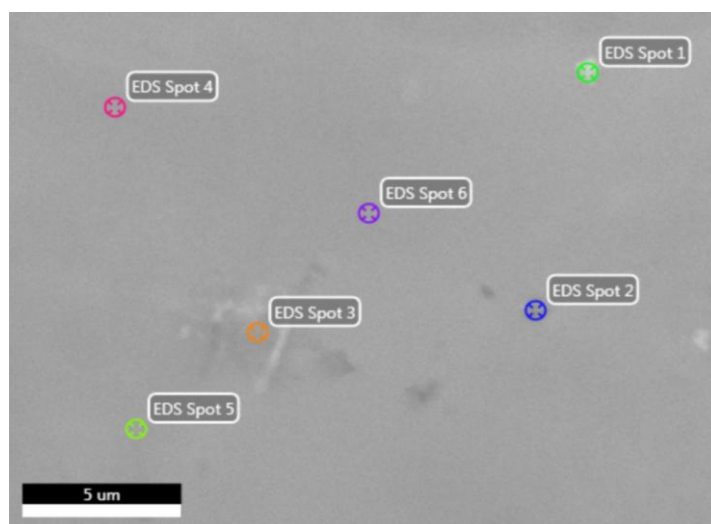


Figure 23: SEM image of the sample with $x = 0.1$ with atomic percent determined at different spots

The atomic percent at different spots is presented in the Table 4.

Table 4: Atomic percent for the sample with $x = 0.1$ at various spots as measured by EDX

	Spot 1 (%)	Spot 2 (%)	Spot 3 (%)	Spot 4 (%)	Spot 5 (%)	Spot 6 (%)	Expected (%)
Ba	14.6	15.2	22.8	14.5	14.4	14.3	14.6
La	0.6	0.4	4.7	0.3	0.4	0.5	0.2
Ga	28.6	28.4	30.3	28.8	28.5	28.8	29.6
Ge	56.2	56.0	42.2	56.3	56.7	56.4	55.6

It can be seen from the table above that the atomic percent for the sample with $x = 0.1$ at different spots is close to the expected atomic percent except for Spot 3 which, is an anomaly. Spot 3 has higher concentration of Ba. EDX showed much more homogenous distribution of Ba in the sample because only a small sample area is chosen for EDX analysis and it is qualitative analysis. EPMA is more quantitative.

4.3.2 $x = 0.2$

Mapping of all elements was performed via EDX on the sample with $x = 0.2$ and is presented in Figure 24.

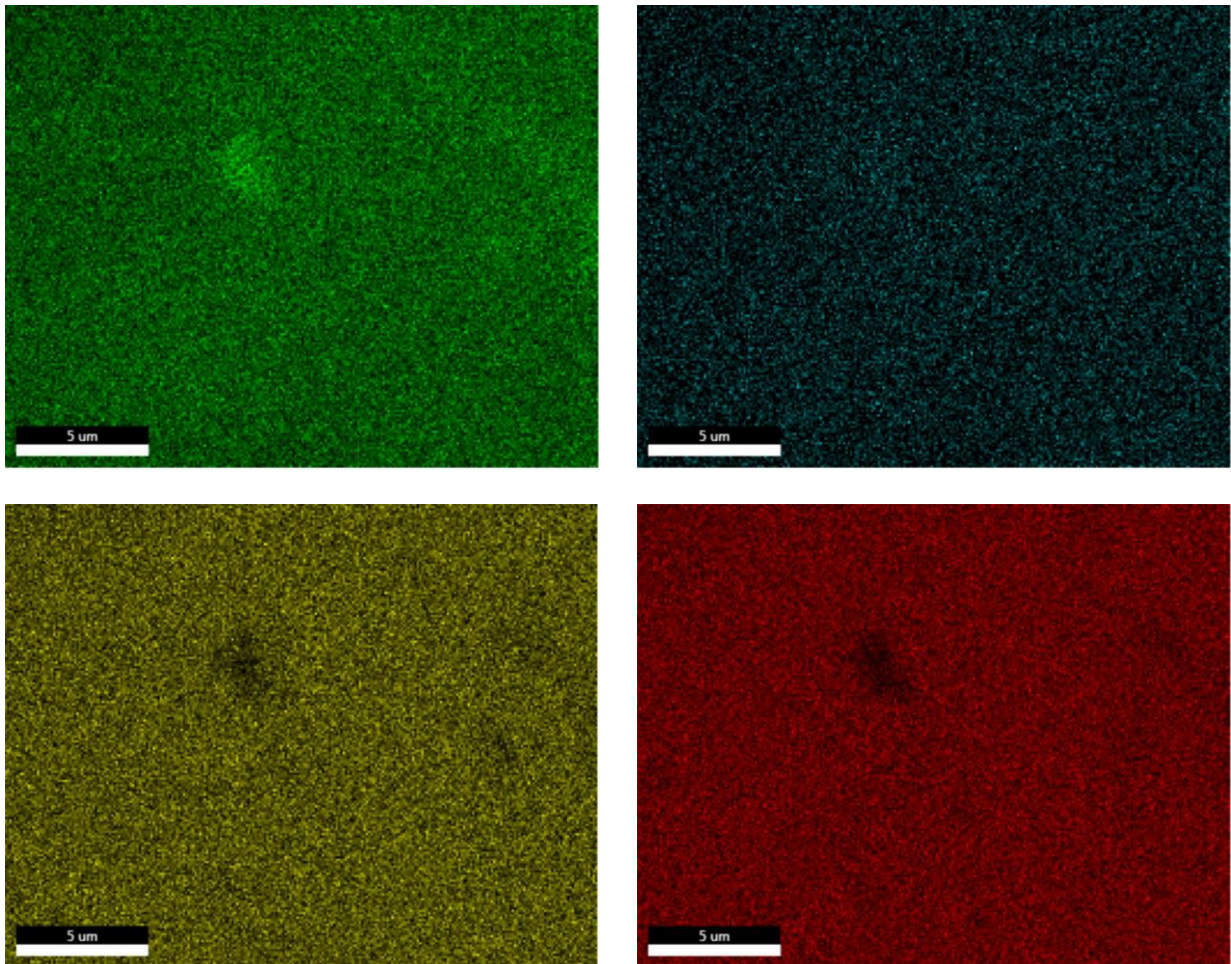


Figure 24: Clockwise from top left mapping of: Ba, La, Ge, Ga

It can be seen from the EDX mapping that all elements are present uniformly throughout the sample. However there is one spot which is Ba rich and Ga, Ge is not present significantly in that spot. This is due to the excess Ba starting amount.

Atomic percent was also measured for the sample with $x = 0.2$ via EDX. The SEM image of the sample is presented in Figure 25.

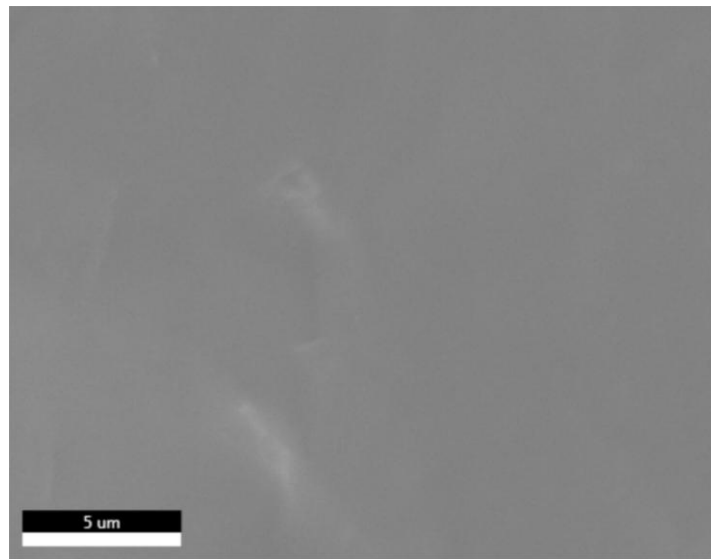


Figure 25: SEM image of the sample with $x = 0.2$

The atomic percent for the overall sample is presented in the Table 5.

Table 5: Atomic percent for the sample with $x = 0.2$ measured by EDX

	Overall (%)	Expected (%)
Ba	13.7	14.6
La	0.5	0.2
Ga	28.7	29.6
Ge	57.1	55.6

Table 5 shows that the atomic percent of all elements is close to the expected percentage.

4.4 EPMA

4.4.1 $x = 0.1$

EPMA was used to measure atomic composition for the sample with $x = 0.1$. The results are presented in Table 6. Standard deviations are shown in parentheses.

Table 6: Atomic composition (in %) for the sample with $x = 0.1$ as measured by EPMA

	Spot 1	Spot 2	Spot 3	Spot 4	Spot 5	Spot 6	Spot 7	Spot 8	Spot 9	Spot 10	Avg.	Expected
Ba	15.7	15.5	15.5	15.5	15.5	15.5	15.6	15.7	15.5	15.6	15.6 (0.08)	14.6
La	0.1	0.2	0.2	0.2	0.2	0.2	0.1	0.2	0.1	0.2	0.2 (0.05)	0.2
Ga	25.6	25.8	25.9	25.7	26	25.6	25.8	25.7	26	25.5	25.8 (0.16)	29.6
Ge	58.6	58.5	58.3	58.7	58.4	58.7	58.5	58.4	58.4	58.7	58.5 (0.14)	55.6

From the EPMA results, it can be deduced that Ba is present in slightly higher amount than expected. This is most likely barium oxide. This is due to excess Ba used initially. La on average is present as expected. Ga concentration on average is lower than expected while Ge concentration on average is higher than expected. However, the total Ga/Ge concentration is similar to the expected total Ga/Ge concentration. The characteristic X-ray energies for Ga and Ge are close: $K\alpha$ for Ga is 9.241 eV and 9.874 eV for Ge and $L\alpha$ for Ga is 1.098 eV and for Ge it is 1.188 eV which might have caused these inaccuracies.

4.4.2 $x = 0.2$

Table 7 displays the atomic composition measured by EPMA. Standard deviation is included in the parentheses.

Table 7: Atomic composition (in %) for the sample with $x = 0.2$ as measured by EPMA

	Spot 1	Spot 2	Spot 3	Spot 4	Spot 5	Spot 6	Spot 7	Spot 8	Spot 9	Spot 10	Avg. (0.06)	Expected
Ba	15.6	15.7	15.8	15.7	15.8	15.7	15.7	15.7	15.7	15.6	15.7 (0.06)	14.4
La	0.2	0.2	0.2	0.2	0.2	0.2	0.1	0.2	0.1	0.2	0.2 (0.04)	0.4
Ga	26.5	27	26.9	26.8	26.6	27	26.9	26.9	26.6	26.9	26.8 (0.17)	29.6
Ge	57.8	57.1	57.1	57.3	57.5	57.1	57.3	57.3	57.6	57.4	57.3 (0.22)	55.6

Similar to the sample with $x = 0.1$, it can be seen that Ba concentration is slightly higher than expected and La concentration is close to expected. Ga concentration on average is lower than expected while Ge concentration on average is higher than expected. However, the total Ga/Ge concentration is similar to the expected total Ga/Ge concentration.

4.5 Physical Property Measurements

4.5.1 Thermal Conductivity

Thermal conductivity was measured on the La samples as well as the sample pellets with $x = 0$. The results are presented in Figure 26.

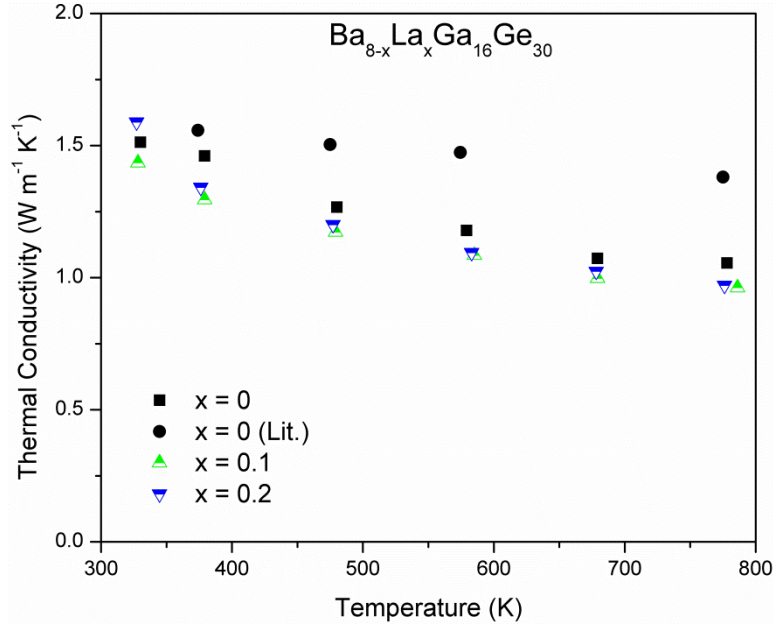


Figure 26: Thermal conductivity for La samples

Around 330 K, the thermal conductivity value for the sample with $x = 0$ is $1.51 \text{ W m}^{-1}\text{K}^{-1}$, for the sample with $x = 0.1$ it is slightly lower at $1.44 \text{ W m}^{-1}\text{K}^{-1}$, and for the sample with $x = 0.2$, it is $1.59 \text{ W m}^{-1}\text{K}^{-1}$. The thermal conductivity values around 780 K are 1.06, 0.96 and $0.97 \text{ W m}^{-1}\text{K}^{-1}$ for the samples with $x = 0$, $x = 0.1$ and $x = 0.2$ respectively.

Compared to literature, all samples display lower thermal conductivity except at around 400 K.⁴⁶ Literature sample starts at $1.56 \text{ W m}^{-1}\text{K}^{-1}$ at 374 K and ends with $1.38 \text{ W m}^{-1}\text{K}^{-1}$ at 775 K. The temperature dependence on thermal conductivity is evident in all samples. As the temperature increases, the thermal conductivity decreases. This is because as the temperature increases, the vibration of the atoms increases which causes scattering of phonons thereby reducing thermal conductivity. It can also be seen that addition of La causes reduction of thermal conductivity. Except for the first value of the sample with $x = 0.2$, all values of La samples are display lower thermal conductivity than the sample with $x = 0$, although the

difference is within error. Increasing La content does not seem to affect thermal conductivity as both La samples display quite similar values from the second point onwards.

4.5.2 Electrical Conductivity

Electrical conductivity was measured along with Seebeck coefficient after cutting a rectangular bar from the hot pressed pellets. The electrical conductivity of the La samples is shown in Figure 27.

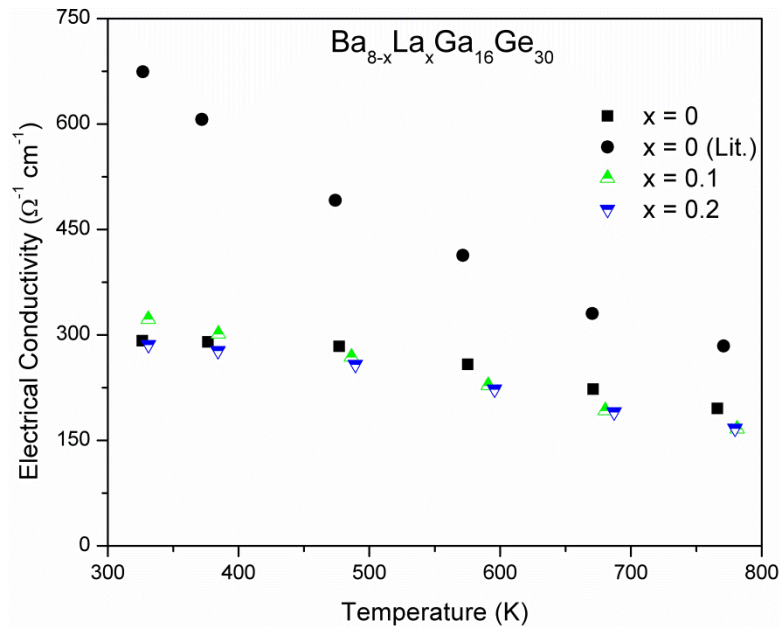


Figure 27: Electrical conductivity of La samples

At ~330 K, BGG displays an electrical conductivity of $292 \Omega^{-1}\text{cm}^{-1}$; the sample with $x = 0.1$ has electrical conductivity of $322 \Omega^{-1}\text{cm}^{-1}$ while the sample with $x = 0.2$ has a value of $286 \Omega^{-1}\text{cm}^{-1}$. The electrical conductivity values at ~780 K for BGG, samples with $x = 0.1$ and $x = 0.2$ are $195 \Omega^{-1}\text{cm}^{-1}$, $166 \Omega^{-1}\text{cm}^{-1}$ and $167 \Omega^{-1}\text{cm}^{-1}$ respectively.

Compared to La free references sample, all samples display lower electrical conductivity at all temperatures.⁴⁶ Literature sample has an electrical conductivity of $674 \Omega^{-1}\text{cm}^{-1}$ and decreases to $284 \Omega^{-1}\text{cm}^{-1}$ at 770 K. The literature sample was pressed using SPS which leads to a denser pellet and subsequently better electrical conductivity properties.

All samples behave as heavily doped semiconductors. With increasing temperature, the electrical conductivity decreases. This is due to increased vibration of the atoms at higher temperatures which causes more collisions with charge carrying particles. The relaxation for charge carriers is thereby reduced, which results in lower mobility, which in turn leads to a lower electrical conductivity.

It is also notable that the addition of La causes a decrease in electrical conductivity in general. This is more evident at higher temperatures. Addition of La should increase carrier concentration theoretically but it also seems to lower mobility which would explain the decrease in electrical conductivity. Increasing La content does not seem to affect electrical conductivity, which is more evident at higher temperatures.

4.5.3 Seebeck coefficient

Seebeck coefficient of La samples is displayed in Figure 28.

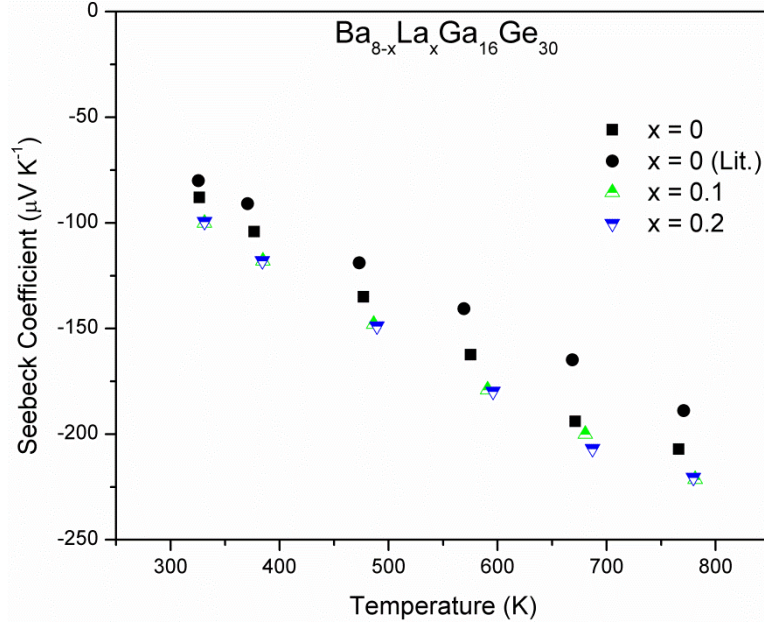


Figure 28: Seebeck coefficient of La clathrates

The values for Seebeck coefficient at ~330 K are $-88 \mu\text{V K}^{-1}$, $-100 \mu\text{V K}^{-1}$ and $-99 \mu\text{V K}^{-1}$ for BGG, samples with $x = 0.1$ and $x = 0.2$ in order. The final Seebeck coefficient values at ~780 K are -207 for BGG, $-221 \mu\text{V K}^{-1}$, for sample with $x = 0.1 \mu\text{V K}^{-1}$, and $-220 \mu\text{V K}^{-1}$ for sample with $x = 0.2$.

The Seebeck coefficient of all 3 samples is lower than the literature sample.⁴⁶ The literature sample has a Seebeck coefficient of $-80 \mu\text{V K}^{-1}$ at 325 K which increases to $-189 \mu\text{V K}^{-1}$ at 770 K. All three samples display *n*-type behaviour with increasing Seebeck coefficient as the temperature increases. Introducing La within the structure causes a slight increase in Seebeck coefficient although it is within error. Increasing La concentration does not seem to affect Seebeck Coefficient as data points for the samples with $x = 0.1$ and $x = 0.2$ are quite similar to each other.

Using the Seebeck coefficient, Lorenz number can be calculated for all samples, and then using the Lorenz number and electrical conductivity, the lattice thermal conductivity can be estimated using equation 1.8, 1.9 and 1.10. Since acoustic phonon scattering is the dominant scattering mechanism, $\lambda = 0$. The Lorenz number for all La samples is presented in the Figure 29 along with the literature sample.

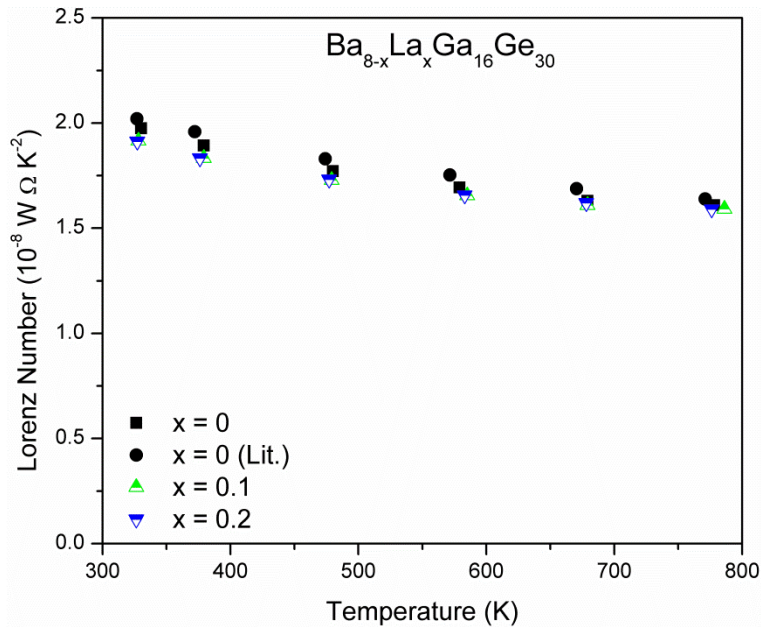


Figure 29: Lorenz numbers of La samples

The lattice thermal conductivity calculated from the Lorenz numbers is presented in Figure 30.

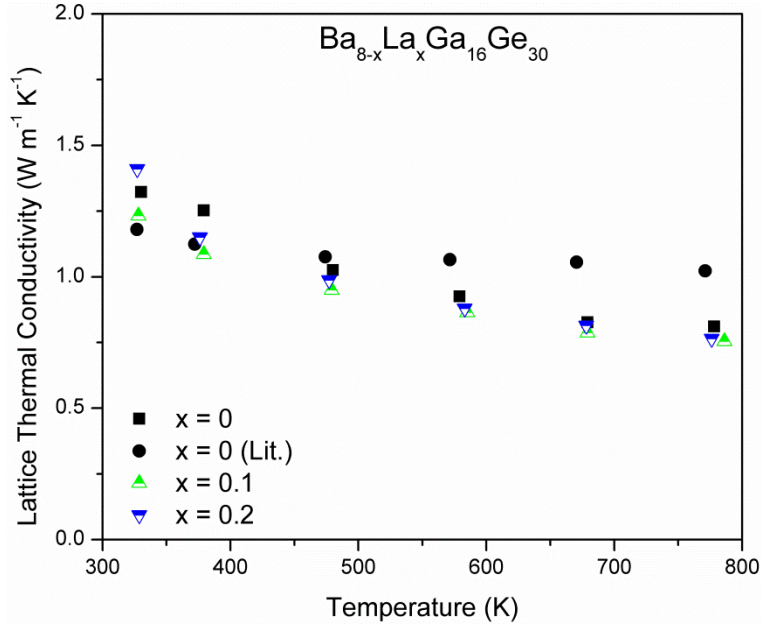


Figure 30: Lattice thermal conductivity for La samples

For the sample with $x = 0$, the lattice thermal conductivity is $1.32 \text{ W m}^{-1}\text{K}^{-1}$ at 330 K which decreases to $0.8 \text{ W m}^{-1}\text{K}^{-1}$ at 778 K. Samples with $x = 0.1$ and $x = 0.2$ have similar trends to the sample with $x = 0$. This suggests that inclusion of La has no change in the lattice thermal conductivity.

Compared to literature, all samples display similar lattice thermal conductivity values until around 500 K. Beyond this temperature, the lattice thermal conductivity of literature sample is higher than the other samples.⁴⁶

4.5.4 Power Factor

Combining the electrical conductivity and Seebeck coefficient, power factor can be obtained. The numerator in the ZT equation is referred to as power factor (PF) and has the formula $PF = S^2\sigma$. The power factor for La samples is presented in Figure 31.

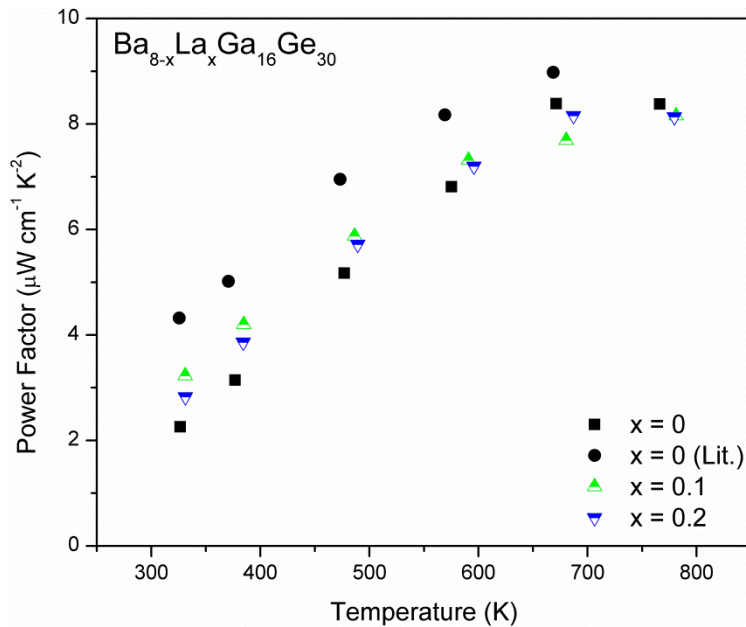


Figure 31: Power factor of La clathrates

The power factor for the sample with $x = 0$ increases from $2.3 \mu\text{W cm}^{-1} \text{K}^{-2}$ at 330 K to $8.4 \mu\text{W cm}^{-1} \text{K}^{-2}$ at 780 K. For the sample with $x = 0.1$, power factor starts at $3.2 \mu\text{W cm}^{-1} \text{K}^{-2}$ at 330 K and increases to $8.2 \mu\text{W cm}^{-1} \text{K}^{-2}$ at 780 K. For the sample with $x = 0.2$, power factor increases from $2.8 \mu\text{W cm}^{-1} \text{K}^{-2}$ at 330 K to $8.1 \mu\text{W cm}^{-1} \text{K}^{-2}$ at 780 K. All samples display similar power factors in general. The literature sample has higher power factor than all other samples due to a higher electrical conductivity.

4.5.5 Figure-of-merit

Combining the property measurements mentioned above, the figure-of-merit for these samples was obtained as shown in the next figure. The temperature of thermal conductivity was used since the temperatures of Seebeck coefficient and electrical conductivity measurement was

close to the temperature of thermal conductivity. Figure-of-merit for La samples is displayed in Figure 32.

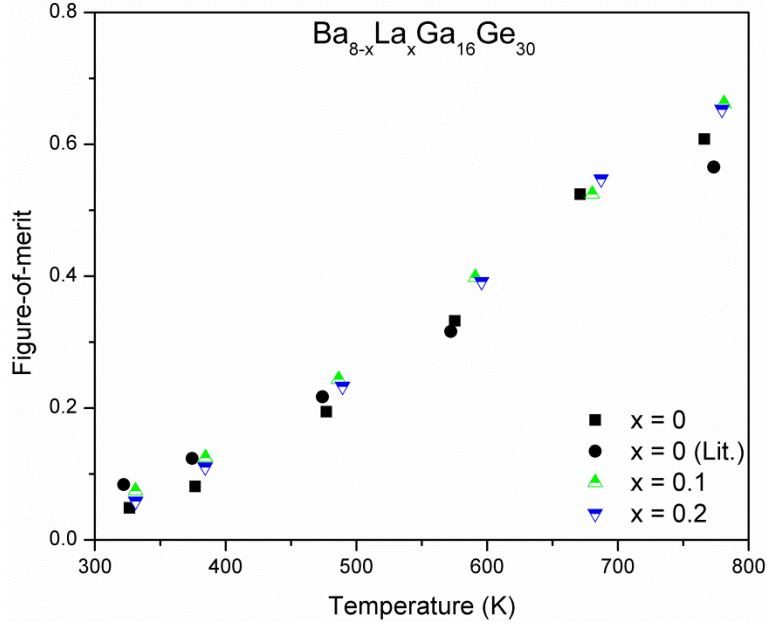


Figure 32: Figure-of-merit for La samples

Figure-of-merit for the sample with $x = 0$ at ~ 330 K is 0.05 which increases to 0.61 at ~ 780 K. The sample with $x = 0.1$ displays a figure-of-merit of 0.07 at ~ 330 K and 0.66 at ~ 780 K. As for the sample with $x = 0.2$, it has a figure-of-merit of 0.06 at ~ 330 K and 0.65 at ~ 780 K. The general trend for all samples is an increase in figure-of-merit with increasing temperature which is caused by increase in power factor and reduction in thermal conductivity.

Addition of La in the clathrates generally causes an increase in figure-of-merit although it is within error. For figure-of-merit, an error of around 8% to 10% is considered. As with all other property measurements, increasing La concentration does not seem to affect figure-of-merit since samples with $x = 0.1$ and $x = 0.2$ display similar trends.

4.6 Conclusion

La double filled clathrates were synthesized and physical property measurements were performed on samples with $x = 0.1$ and $x = 0.2$. PXRD revealed phase pure samples. EPMA and EDX data suggests that the atomic composition of the samples is close to expected results. Double filling clathrates with Ba and La causes a decrease in thermal conductivity, decrease in electrical conductivity and increase in Seebeck coefficient in general. The end result is an improvement of the thermoelectric figure-of-merit. Without double filling, the sample with $x = 0$ has a maximum ZT of 0.61 at 780 K while samples with $x = 0.1$ and $x = 0.2$ have a ZT of 0.66 and 0.65 respectively at 780 K. The sample with $x = 0.1$ appears to be the best thermoelectric material in this case with an improvement of 8% in ZT but it should be noted that it lies within experimental error.

5. Eu containing clathrates

All Eu samples were synthesized as mentioned earlier in Section 3.1

For Eu samples, $\text{Ba}_{8-x}\text{Eu}_x\text{Ga}_{16}\text{Ge}_{30}$ with values of x ranging from 0 to 0.5 were synthesized successfully with large enough samples to perform physical property measurements on. $x = 0.5$ seemed to be the solubility limit for this phase as shown in Figure 33 below.

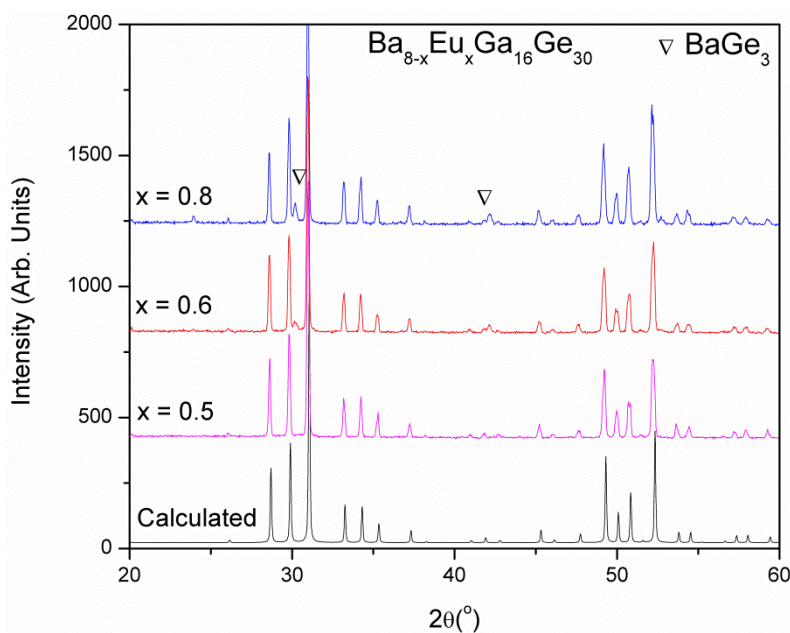


Figure 33: Solubility limit for Eu containing clathrates

As is evident from Figure 33, BaGe_3 starts to appear as a side product in the sample with $x = 0.6$, and its concentration increases for the sample with $x = 0.8$.

5.1 XRD Analysis

5.1.1 PXRD Analysis

$\text{Ba}_{8-x}\text{Eu}_x\text{Ga}_{16}\text{Ge}_{30}$ samples with $x = 0$ to 0.5 were determined to be phase-pure according to powder X-ray diffraction patterns. The diffraction patterns were obtained on an Inel powder diffractometer, which is equipped with a position-sensitive detector and utilizes $\text{Cu } K\alpha_1$ radiation. After synthesis, XRD analysis was performed on these samples. The powder patterns are compared to the reference $\text{Ba}_8\text{Ga}_{16}\text{Ge}_{30}$ sample as shown in Figure 34.

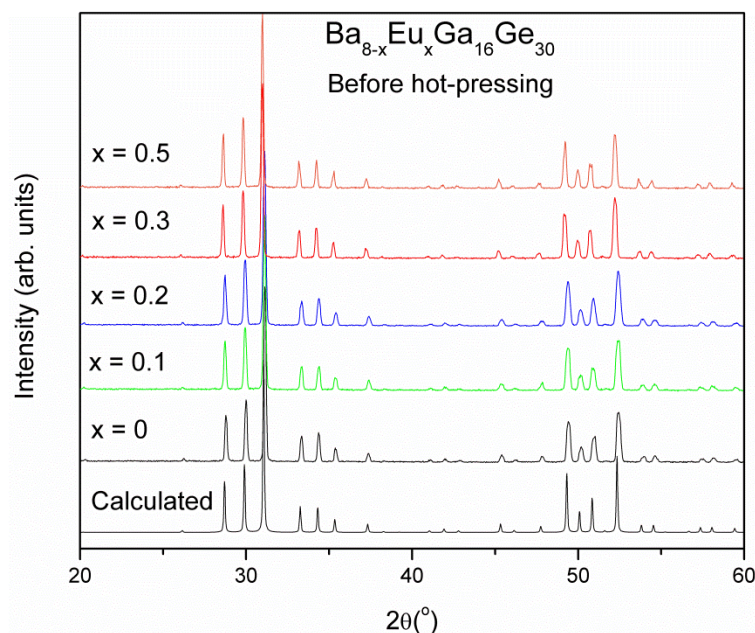


Figure 34: XRD results for Eu containing clathrates before hot pressing

All pure samples were hot-pressed into circular pellets with a 12.7 mm diameter and a thickness of ~ 2 mm under argon flow inside a graphite die using the FR-210-30T hot press from Oxy-Gon Industries. The optimized pressing conditions for all samples were 77 MPa at 1100 K with a 2 h dwell time. The densities for all samples were measured using Archimedes principle

which resulted in >96% theoretical densities for all samples. Once the hot pressed pellet was obtained, physical properties were measured. The samples have been labelled with the appropriate number which corresponds to the x value.

After all physical property measurements were completed, XRD analysis was performed again. The post-measurement XRD analysis is presented in the Figure 35.

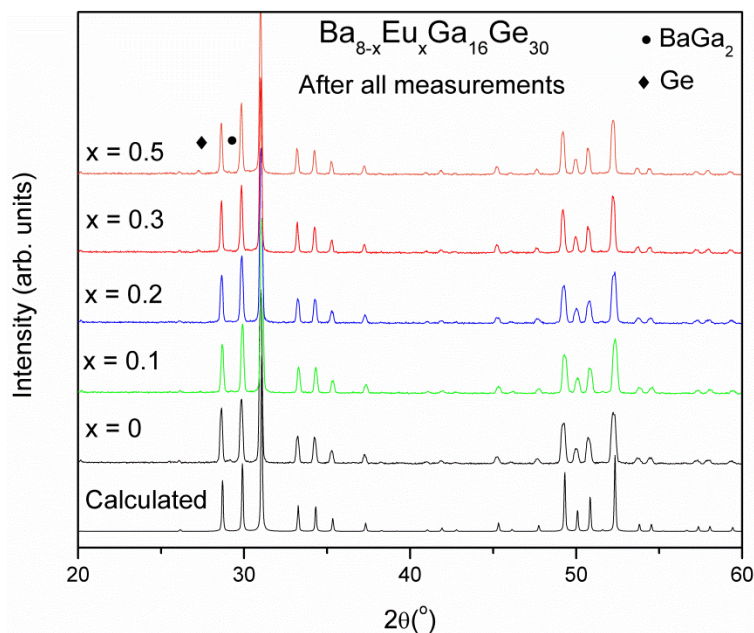


Figure 35: XRD analysis for Eu clathrates after all measurements

It can be seen samples are partly decomposing during either the measurements or hot pressing with Ge and BaGa_2 as the main side products found after XRD analysis.

5.1.2 Single Crystal

Single crystal analysis was done on samples with $x = 0.1$, $x = 0.3$ and $x = 0.4$. Two models were used. In one model, Eu occupancy was refined on both $2a$ and $6d$ Wyckoff sites. The results of that model are displayed in Table 8.

Table 8: Crystallographic details of $\text{Ba}_{8-x}\text{Eu}_x\text{Ga}_{16}\text{Ge}_{30}$ with Eu placed on both $2a$ and $6d$ Wyckoff positions

Nominal formula	$\text{Ba}_{7.9}\text{Eu}_{0.1}\text{Ga}_{16}\text{Ge}_{30}$	$\text{Ba}_{7.7}\text{Eu}_{0.3}\text{Ga}_{16}\text{Ge}_{30}$	$\text{Ba}_{7.6}\text{Eu}_{0.4}\text{Ga}_{16}\text{Ge}_{30}$
Refined Eu content	$\text{Eu}_{0.52(13)}$	$\text{Eu}_{0.56(14)}$	$\text{Eu}_{0.60(15)}$
Crystal system	Cubic	Cubic	Cubic
Space group	$Pm\bar{3}n$	$Pm\bar{3}n$	$Pm\bar{3}n$
a [Å]	10.7772(1)	10.77587(6)	10.77630(1)
V [Å ³]	1251.75(2)	1251.287(12)	1251.44(2)
Z	1	1	1
$R1 \setminus wR2$ (all data)	0.011 \ 0.022	0.011 \ 0.022	0.012 \ 0.024
occ(Eu1)	0.03(2)	0.05(2)	0.04(2)
occ(Eu2)	0.077(15)	0.077(17)	0.086(18)
$U_{\text{eq}}(A1)/\text{Å}^2$	0.00978(17)	0.00940(19)	0.0093(2)
$U_{\text{eq}}(A2)/\text{Å}^2$	0.03726(18)	0.0378(2)	0.0374(2)
$U_{\text{eq}}(E1)/\text{Å}^2$	0.00802(12)	0.00741(13)	0.00729(14)
$U_{\text{eq}}(E2)/\text{Å}^2$	0.00819(9)	0.00760(10)	0.00751(10)
$U_{\text{eq}}(E3)/\text{Å}^2$	0.00830(9)	0.00775(9)	0.00767(10)

In Table 8, A1 represents Ba and Eu on the $2a$ position and A2 represents Ba and Eu on the $6d$ position while E1, E2 and E3 represent Ga/Ge in their respective Wyckoff positions. The Ga/Ge occupancies were fixed according to the literature.⁶¹ Another important point is that the atomic displacement parameter of the $6d$ position is larger than the $2a$ position. This indicates

that the $6d$ position is acting more as a rattler. The refined Eu content is equal within error for all three single crystals. The lattice parameters are as well quite consistent. The occupancy of Eu1 (occ(Eu1) in the table) has a large standard deviation. Eu1 occupancy is almost 0 within 2 standard deviations.

Another model with Eu only on the $6d$ position was also tried. The results of the refinement are in Table 9.

Table 9: Crystallographic details of Ba $8-x$ Eu x Ga 16 Ge 30 with 2a position occupancy fixed at 0

Nominal formula	Ba _{7.9} Eu _{0.1} Ga ₁₆ Ge ₃₀	Ba _{7.7} Eu _{0.3} Ga ₁₆ Ge ₃₀	Ba _{7.6} Eu _{0.4} Ga ₁₆ Ge ₃₀
Refined Eu content	Eu _{0.45(09)}	Eu _{0.44(10)}	Eu _{0.50(11)}
Crystal system	Cubic	Cubic	Cubic
Space group	$Pm\bar{3}n$	$Pm\bar{3}n$	$Pm\bar{3}n$
a [Å]	10.7772(1)	10.77587(6)	10.77630(1)
V [Å ³]	1251.75(2)	1251.287(12)	1251.44(2)
Z	1	1	1
R1 \ wR2 (all data)	0.011 / 0.022	0.011/0.023	0.012 \ 0.024
occ(Eu1)	fixed at 0	fixed at 0	fixed at 0
occ(Eu2)	0.074(15)	0.073(17)	0.083(18)
$U_{eq}(A1)/\text{Å}^2$	0.00962(12)	0.00910(13)	0.00904(13)
$U_{eq}(A2)/\text{Å}^2$	0.03727(18)	0.0378(2)	0.0374(2)
$U_{eq}(E1)/\text{Å}^2$	0.00805(12)	0.00746(13)	0.00733(13)
$U_{eq}(E2)/\text{Å}^2$	0.00822(9)	0.00764(9)	0.00755(10)
$U_{eq}(E3)/\text{Å}^2$	0.00833(9)	0.00780(9)	0.00770(10)

Table 8 and 9 suggest that Eu prefers the $6d$ position. The second model also displays the refined Eu contents being closer to the nominal contents. Neutron diffraction studies in literature

have revealed that the guest atoms are usually off-centre in their positions inside the cages.³⁸ It is likely that Eu being smaller than Ba maybe even more off-centered, which would enhance its role as a rattler thereby scattering phonons more effectively.

5.2 EDX

5.2.1 $x = 0$

EDX mapping was performed on the sample with $x = 0$. The results are shown in the Figure 36.

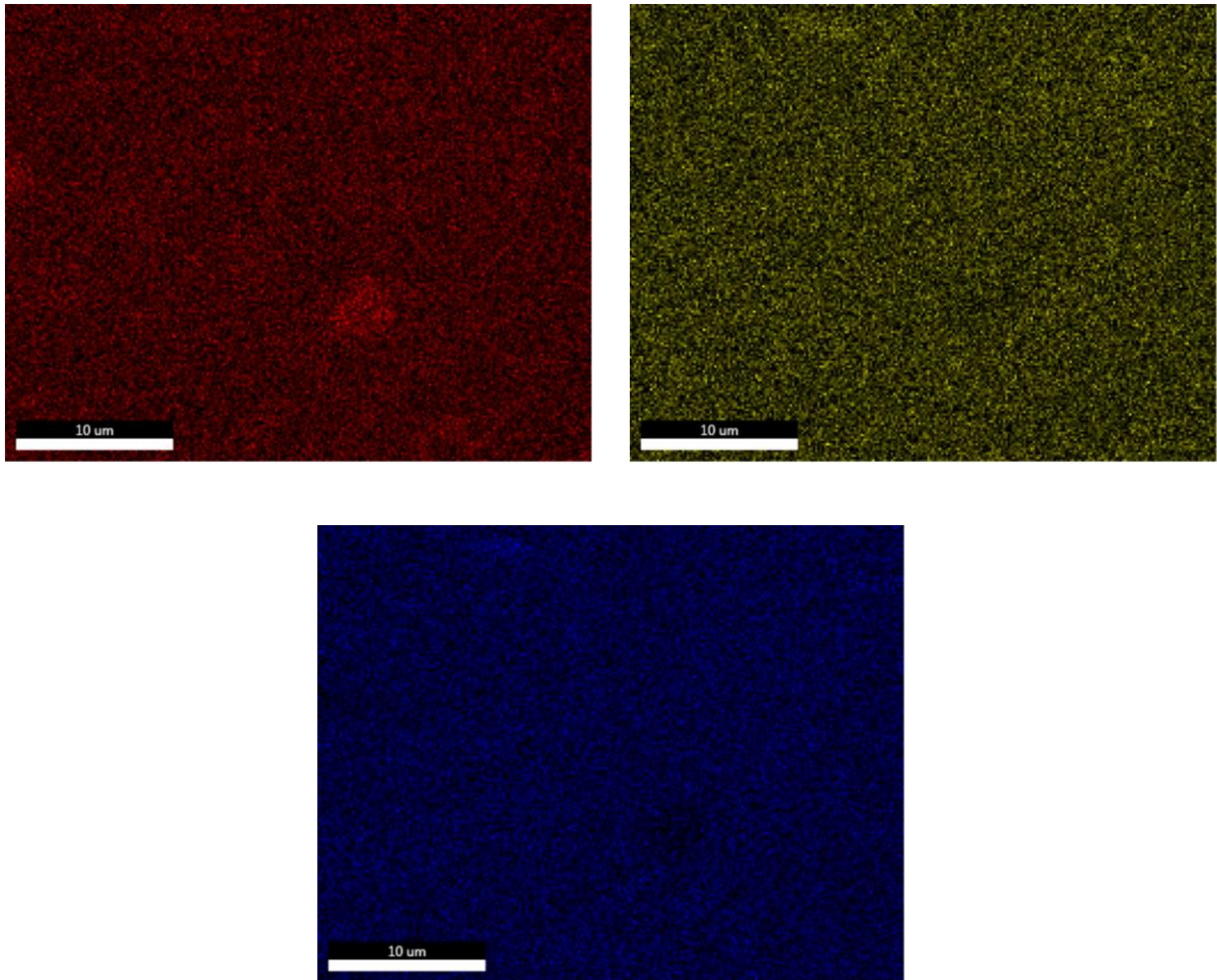


Figure 36: EDX mapping of the sample with $x = 0$. Clockwise from top left: Ba, Ga and Ge

From Figure 36, it can be seen that Ba, Ga and Ge are evenly distributed throughout the sample. There is a slight excess of Ba present. This could be due to the fact that excess Ba was

used at the start. Atomic composition was also measured at various spots within the sample as shown in Figure 37.

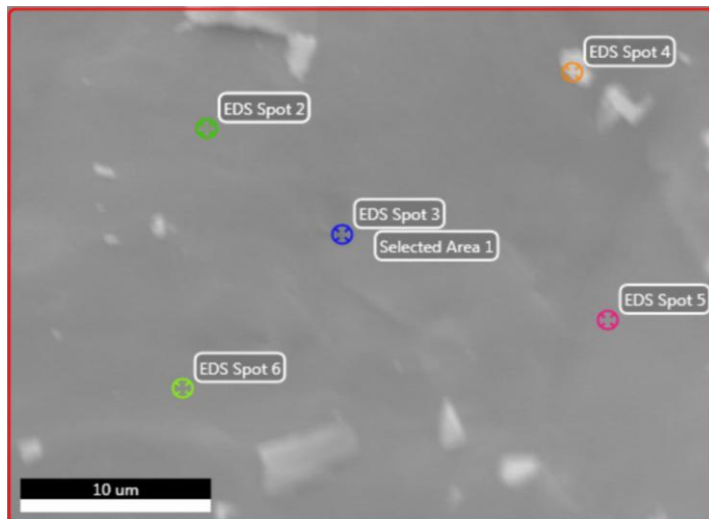


Figure 37: SEM image for the sample with $x = 0$ with atomic percentage at various spots

The atomic composition for the sample with $x = 0$ is presented in Table 10.

Table 10: EDX Spot analysis for the sample with $x = 0$

	Spot 2	Spot 3	Spot 4	Spot 5	Spot 6	Overall	Expected
Ba	15.7	16.9	15.3	15.7	15.8	16.3	14.8
Ga	28.4	27.8	28.3	28.5	28.4	28.4	29.6
Ge	55.9	55.3	56.4	55.8	55.8	55.3	55.6

The atomic composition for Ga and Ge are close to expected. Ba, on the other hand, is present has an atomic composition higher than expected. This is due to excess Ba used during synthesis.

5.2.2 $x = 0.1$

Atomic composition was also measured at various spots within the sample as shown in Figure 38.

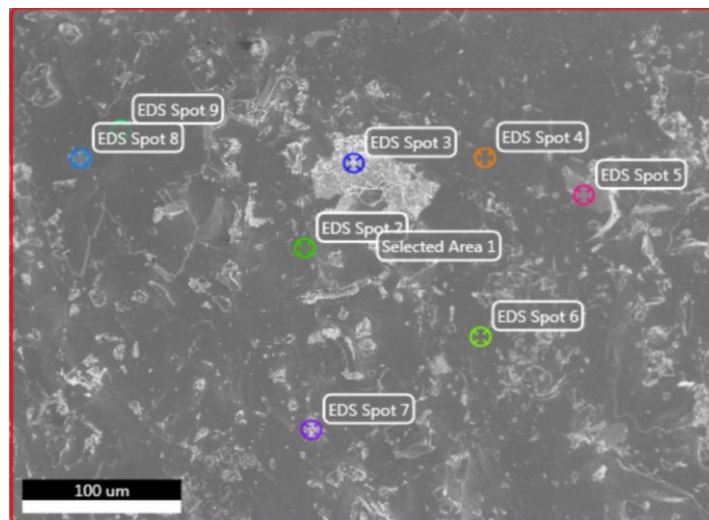


Figure 38: SEM image for the sample with $x = 0.1$

Table 11 shows measured atomic composition at various spots.

Table 11: EDX Spot analysis for the sample with $x = 0.1$

	Spot 2	Spot 3	Spot 4	Spot 5	Spot 6	Spot 7	Spot 8	Spot 9	Overall	Expected
Ba	13.9	49.7	14.9	14.1	14.4	33.7	12.9	13.8	16.8	14.6
Eu	2.5	1.8	1.0	1.3	0.9	1.6	1.2	1.8	1.0	0.2
Ga	23.7	10.6	29.0	27.8	28.5	25.6	28.3	27.8	28.2	29.6
Ge	59.9	37.9	55.1	56.8	56.1	39.1	57.5	56.6	54.0	55.6

As it can be seen from Table 11, overall atomic composition as well as atomic composition of most spots are similar to the expected composition. Ba content is high overall in particular Spots 3 and 7, however, have high Ba content. This suggests that excess Ba is present within the sample.

5.2.3 $x = 0.2$

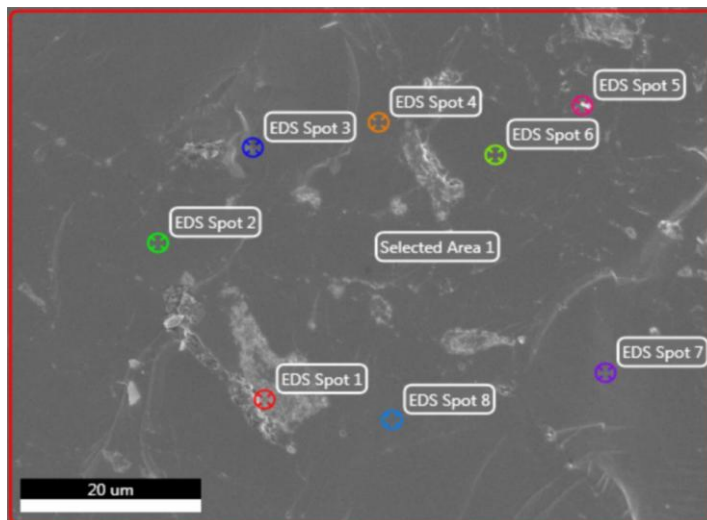


Figure 39: SEM image for the sample with $x = 0.2$

Table 12: EDX Spot analysis for the sample with $x = 0.2$

	Spot 1	Spot 2	Spot 3	Spot 4	Spot 5	Spot 6	Spot 7	Spot 8	Overall	Expected
Ba	29.6	14.9	43.7	14.0	34.0	14.4	13.1	15.4	14.8	14.4
Eu	0.5	0.8	24.3	1.4	1.6	1.1	1.3	0.9	1.0	0.4
Ga	28	28.9	18.2	28.6	13.4	28.4	28.4	28.6	28.1	29.6
Ge	41.9	55.4	13.8	56.0	51.0	56.1	57.2	55.1	56.1	55.6

Most spots in the table above correspond to the expected atomic percent. However Spots 1, 3 and 5 have high Ba content. Again, this is may be due to the usage of excess Ba. Spot 3 also has a very high Eu content, which suggests that Eu is not fully substituting Ba as expected

5.2.4 $x = 0.3$

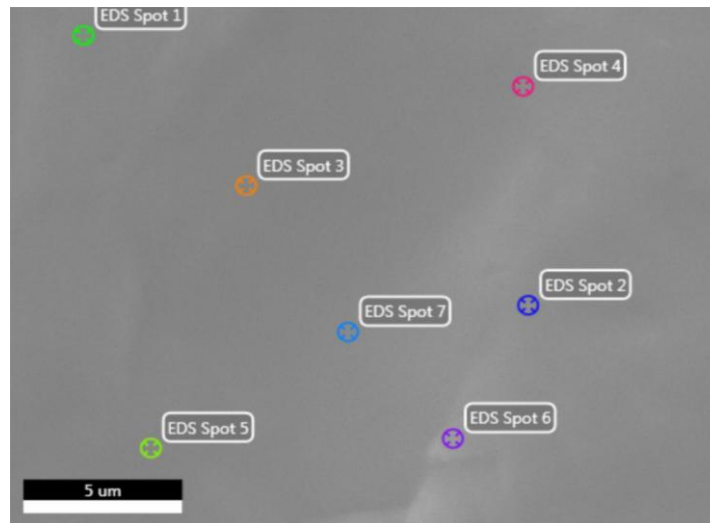


Figure 40: SEM image for the sample with $x = 0.3$

Table 13: EDX Spot analysis for the sample with $x = 0.3$

	Spot 1	Spot 2	Spot 3	Spot 4	Spot 5	Spot 6	Spot 7	Average	Expected
Ba	18.1	15.5	14.3	15.1	16.2	16.8	14.9	15.8	14.2
Eu	0.5	0.3	0.6	0.2	0.6	0.2	0.2	0.4	0.6
Ga	27.0	28.2	28.6	28.4	28.0	27.5	28.3	28.0	29.6
Ge	54.4	56.0	56.6	56.3	55.3	55.5	56.5	55.8	55.6

For the sample with $x = 0.3$, atomic composition of Eu, Ga and Ge are close to expected. Spot 1 shows higher Ba content than normal.

5.3 EPMA

5.3.1 $x = 0$

EPMA was performed on the sample with $x = 0$ to further determine the atomic composition. The table below lists the atomic percent for the sample with $x = 0$ as measured by EPMA. Standard deviations are included in the parentheses.

Table 14: EPMA analysis for the sample with $x = 0$

	Spot 1	Spot 2	Spot 3	Spot 4	Average	Expected
Ba	14.7	14.7	14.7	14.6	14.7 (0.04)	14.8
Ga	30.2	29.9	30.5	30.4	30.3 (0.23)	29.6
Ge	55.1	55.3	54.8	55.0	55.0 (0.18)	55.6

For the sample with $x = 0$, all four spots show atomic percent of the elements as expected within error.

5.3.2 $x = 0.2$

Table 15: EPMA analysis for the sample with $x = 0.2$

	Spot 1	Spot 2	Spot 3	Spot 4	Spot 5	Spot 6	Spot 7	Average	Expected
Ba	14.6	14.6	14.7	14.6	14.6	14.8	14.7	14.7 (0.07)	14.4
Eu	0.1	0.1	0.1	0.1	0.0	0.0	0.1	0.04 (0.05)	0.4
Ga	30.2	30.1	30.4	30.2	30.5	30.4	30.1	30.3 (0.15)	30.2
Ge	55.1	55.2	54.8	55.1	54.9	54.8	55.1	55.0 (0.15)	55.1

For sample with $x = 0.2$, averaged atomic percents of Ba, Ga and Ge are within error of the expected atomic percentages; however the average atomic percent of Eu is lower than expected. This indicates that less than expected Eu is being incorporated into the sample.

5.3.3 $x = 0.5$

Table 16: EPMA analysis for the sample with $x = 0.5$

	Spot 1	Spot 2	Spot 3	Spot 4	Spot 5	Spot 6	Spot 7	Spot 8	Spot 9	Spot 10	Avg.	Expected
Ba	14.7	14.6	14.6	14.5	14.7	14.7	14.8	14.6	14.8	14.5	14.7 (0.10)	13.9
Eu	0.1	0.1	0.1	0.1	0.2	0.1	0.1	0.1	0.1	0.2	0.1 (0.04)	0.9
Ga	29.8	29.7	29.8	29.6	29.7	29.8	29.4	29.7	29.5	29.8	29.7 (0.13)	29.6
Ge	55.4	55.6	55.5	55.8	55.5	55.4	55.8	55.6	55.6	55.5	55.6 (0.13)	55.6

Similar to the sample with $x = 0.2$, averaged atomic percents of Ba, Ga and Ge of the sample with $x = 0.5$ sample are within error of the expected atomic percentages, however the average mass percent of Eu is lower than expected. This indicates that less than expected Eu is being incorporated into the sample. Furthermore, EPMA analysis revealed two spots with 68 and 76 atomic percent Eu. This suggests the presence of europium oxide within this sample.

5.4 Physical Property Measurements

5.4.1 Thermal Conductivity

The thermal conductivity results for Eu samples are presented in Figure 41.

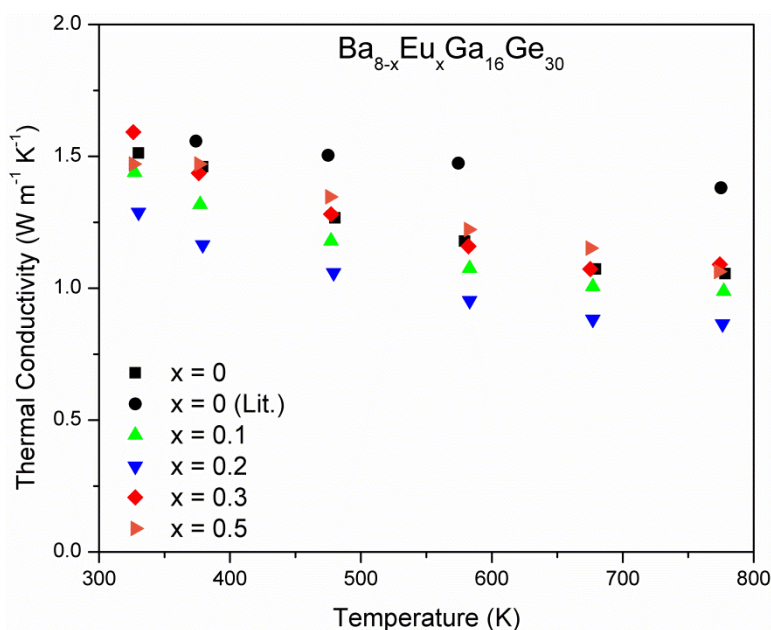


Figure 41: Thermal Conductivity results for Eu containing clathrates

The temperature dependence on thermal conductivity is evident in all samples. As the temperature increases, the thermal conductivity decreases. This is because as the temperature increases, the vibration of the atoms increases which causes scattering of phonons thereby reducing thermal conductivity.

Around 330 K, the thermal conductivity for the sample with $x = 0$ is $1.51 \text{ W m}^{-1} \text{K}^{-1}$. The thermal conductivity of that sample drops to $1.06 \text{ W m}^{-1} \text{K}^{-1}$ at 778 K. Samples with $x = 0.3$ and $x = 0.5$ follow similar trends to the sample with $x = 0$. The sample with $x = 0.1$, however, has slightly lower thermal conductivity throughout the measurement range. For the sample with $x =$

0.1, thermal conductivity is $1.44 \text{ W m}^{-1}\text{K}^{-1}$ at 327 K and decreases to $0.99 \text{ W m}^{-1}\text{K}^{-1}$ at 777 K. The sample with $x = 0.1$ is within error of the sample with $x = 0$. The real interesting result is that of the sample with $x = 0.2$. This sample clearly exhibits lower thermal conductivity than the sample with $x = 0$. For the sample with $x = 0.2$, the thermal conductivity is $1.29 \text{ W m}^{-1}\text{K}^{-1}$ at 330 K and $0.86 \text{ W m}^{-1}\text{K}^{-1}$ at 776 K.

Addition of Eu seems to lower the thermal conductivity up until $x = 0.2$. Beyond that, the thermal conductivity is unaffected by additional Eu input, possibly because the real solubility limit has been reached according to the EPMA data. The reason for reduction in thermal conductivity is due to the enhanced phonon scattering caused by a mass fluctuation upon substitution of Ba by Eu. All samples exhibit lower thermal conductivity when compared to the literature sample with $x = 0$. Literature sample starts at $1.56 \text{ W m}^{-1}\text{K}^{-1}$ at 374 K and ends with $1.38 \text{ W m}^{-1}\text{K}^{-1}$ at 775 K.⁴⁶

5.4.2 Electrical Conductivity

All samples behave as heavily doped semiconductors (Figure 42). With increasing temperature, the electrical conductivity decreases. This is due to increased vibration of the atoms at higher temperatures which causes more collisions with charge carrying particles. The mean free path of the charge carriers is thereby reduced which reduces the mobility of the carriers, in turn leading to a lower electrical conductivity.

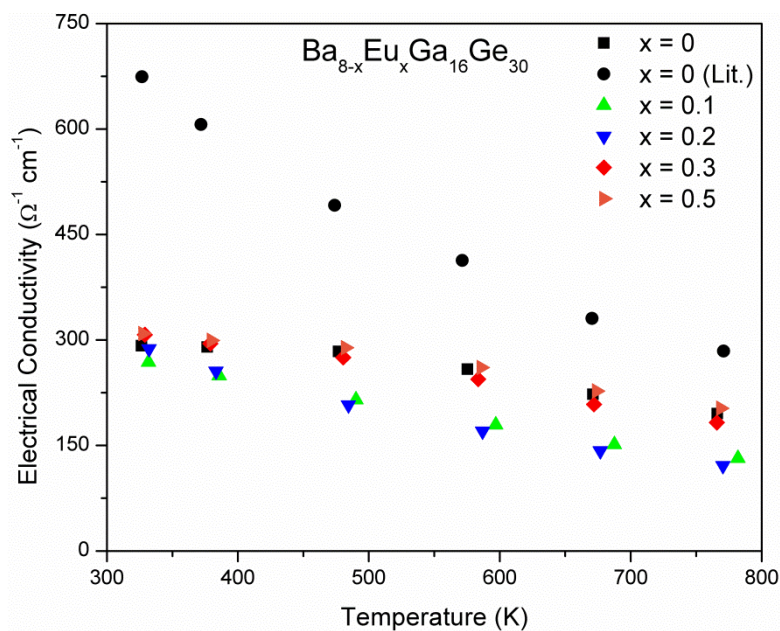


Figure 42: Electrical conductivity of Eu containing clathrates

At ~330 K, the sample with $x = 0$ displays an electrical conductivity of $292 \Omega^{-1} \text{ cm}^{-1}$ and at 780 K, the electrical conductivity drops to $195 \Omega^{-1} \text{ cm}^{-1}$. Samples with $x = 0.3$ and $x = 0.5$ follow a similar pattern to the samples with $x = 0$. The sample with $x = 0.1$ has an electrical conductivity of $268 \Omega^{-1} \text{ cm}^{-1}$ at ~330 K which decreases to $132 \Omega^{-1} \text{ cm}^{-1}$ at 780 K. The sample with $x = 0.2$ displays similar electrical conductivity values to sample with $x = 0.1$ with $287 \Omega^{-1} \text{ cm}^{-1}$ at 330 K and $121 \Omega^{-1} \text{ cm}^{-1}$

It seems that increasing Eu decreases electrical conductivity up until $x = 0.2$. Beyond $x = 0.2$, Eu samples display similar electrical conductivity to the sample with $x = 0$. The decrease in electrical conductivity may be attributed to the decrease in mobility, since it is predicted that

carrier concentration would remain the same because Eu and Ba both would have an oxidation state of +2.

Comparing to literature, all samples exhibit much lower electrical conductivity. Literature sample has an electrical conductivity of $674 \Omega^{-1}\text{cm}^{-1}$ and decreases to $284 \Omega^{-1}\text{cm}^{-1}$ at 770 K. This could be due to the literature using SPS for hot pressing which gives better density compared to hot pressing.⁴⁶

5.4.3 Seebeck Coefficient

The Seebeck coefficient data for Eu samples are presented in Figure 43.

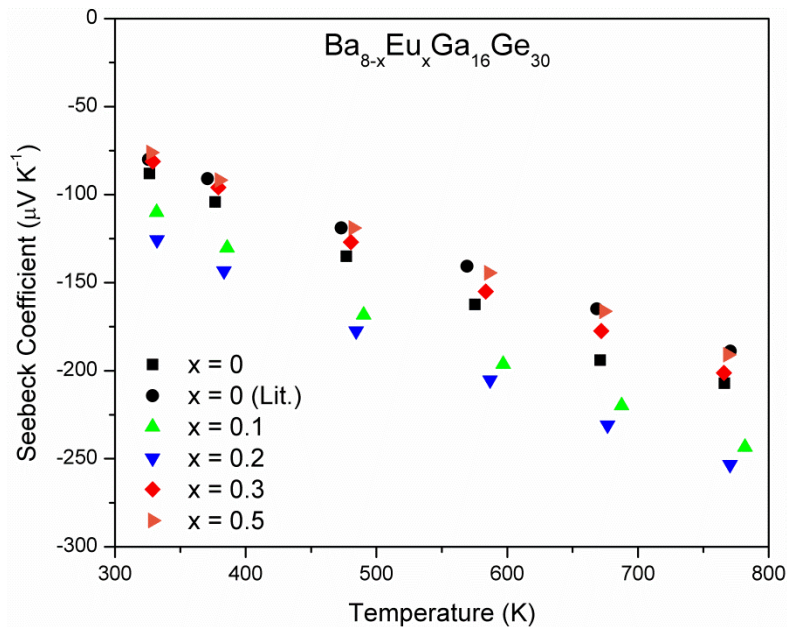


Figure 43: Seebeck coefficient for Eu containing clathrates

All samples display *n*-type behaviour with increasing Seebeck coefficient as the temperature increases. For the sample with $x = 0$, the Seebeck coefficient is $-88 \mu\text{V K}^{-1}$ at 330 K

which increases to $-207 \mu\text{V K}^{-1}$ at 766 K. Samples with $x = 0.1$ and $x = 0.2$ have higher Seebeck coefficient values than the sample with $x = 0$, while samples with $x = 0.3$ and $x = 0.5$ have lower Seebeck coefficient.

Comparing to literature, the sample with $x = 0$ synthesized here has higher Seebeck coefficient than literature. The literature sample has a Seebeck coefficient of $-80 \mu\text{V K}^{-1}$ at 325 K which increases to $-189 \mu\text{V K}^{-1}$ at 770 K.⁴⁶

Using the Seebeck coefficient, Lorenz number can be calculated for all samples, and then using the Lorenz number and electrical conductivity, the lattice thermal conductivity can be estimated using equation 1.8, 1.9 and 1.10. Since acoustic phonon scattering is the dominant scattering mechanism, $\lambda = 0$. The Lorenz number for all La samples is presented in the Figure 44 along with the literature sample.

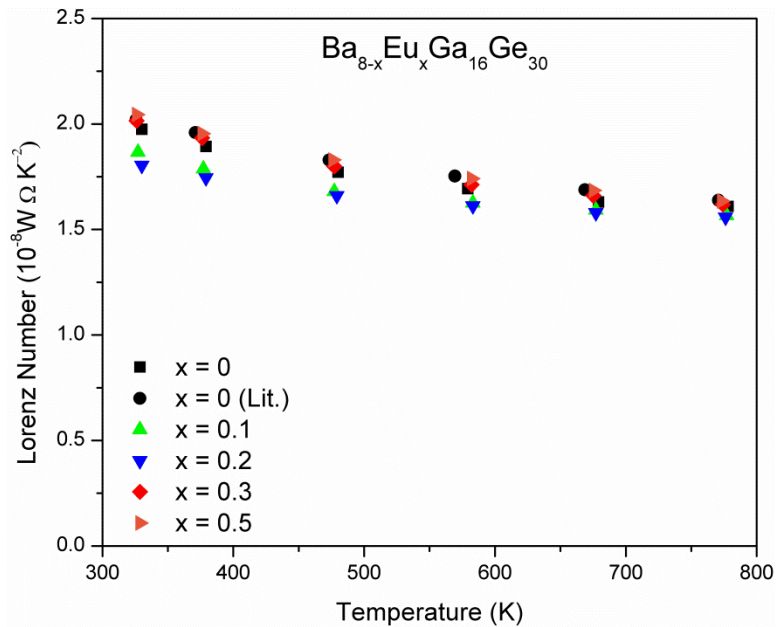


Figure 44: Lorenz number for Eu containing clathrates

Figure 44 shows that the Lorenz number is quite similar in all samples.

The lattice thermal conductivity calculated from the Lorenz numbers is presented in Figure 45.

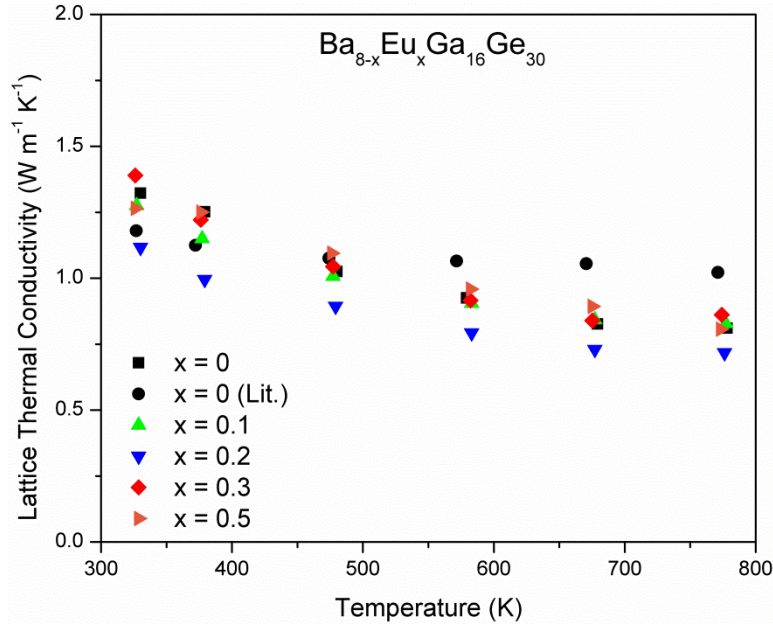


Figure 45: Lattice thermal conductivity for Eu containing clathrates

For the sample with $x = 0$, the lattice thermal conductivity at 330 K is $1.32 \text{ W m}^{-1}\text{K}^{-1}$ which decreases to $0.8 \text{ W m}^{-1}\text{K}^{-1}$ at 778 K. Samples with $x = 0.1$, $x = 0.3$ and $x = 0.5$ display similar lattice thermal conductivity trends as the sample with $x = 0$ sample. The sample with $x = 0.2$ exhibits lower thermal conductivity than the rest of the samples here, starting with a lattice thermal conductivity of $1.12 \text{ W m}^{-1}\text{K}^{-1}$ at 330 K which drops to 0.72 at 776K.

Compared to literature, all samples with the exception of the sample with $x = 0.2$ up to $\sim 500 \text{ K}$ display similar lattice thermal conductivity values. Beyond 500K, literature lattice thermal conductivity values are higher than the rest of the samples.⁴⁶

5.4.4 Power Factor

Combining the electrical conductivity and Seebeck coefficient, power factor can be obtained. The numerator in the ZT equation is referred to as power factor (PF) and has the formula $PF = S^2\sigma$. The power factor for Eu samples is presented in Figure 46.

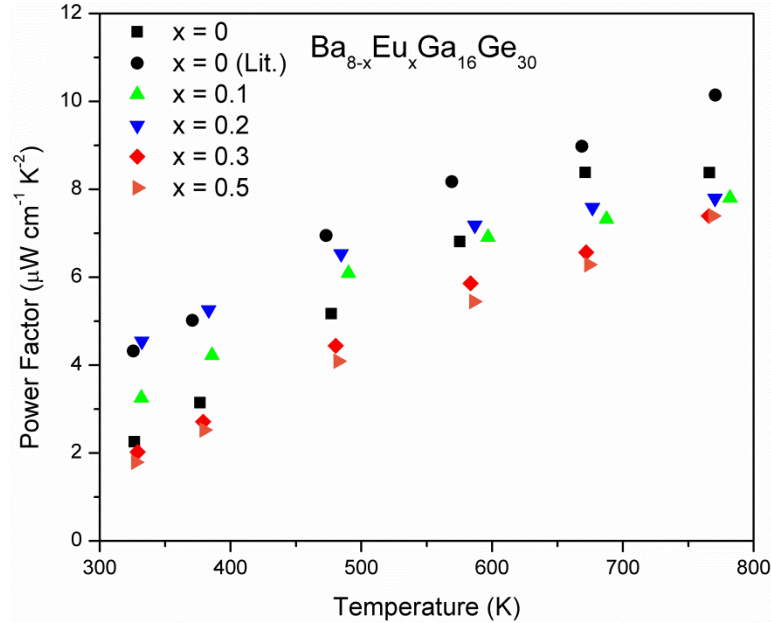


Figure 46: Power Factor for Eu containing clathrates

The power factor for the sample with $x = 0$ increases from $2.3 \mu\text{W cm}^{-1} \text{K}^{-2}$ at 330 K to $8.4 \mu\text{W cm}^{-1} \text{K}^{-2}$ at 780 K. Samples with $x = 0.3$ and $x = 0.5$ generally display lower power factor than the sample with $x = 0$. The sample with $x = 0.1$ starts out with a higher power factor than the sample with $x = 0$ with $3.3 \mu\text{W cm}^{-1} \text{K}^{-2}$ at 330 K but has a lower power factor than the sample with $x = 0$ at 780 K with $7.8 \mu\text{W cm}^{-1} \text{K}^{-2}$. Similarly, for the sample with $x = 0.2$, power factor at 330 K is $4.5 \mu\text{W cm}^{-1} \text{K}^{-2}$ which is higher than the sample with $x = 0$ but at 770 K it drops below the sample with $x = 0$ to $7.8 \mu\text{W cm}^{-1} \text{K}^{-2}$.

The literature sample with $x = 0$ generally has a higher power factor than all samples due to higher electrical conductivity.⁴⁶

5.4.5 Figure-of-merit

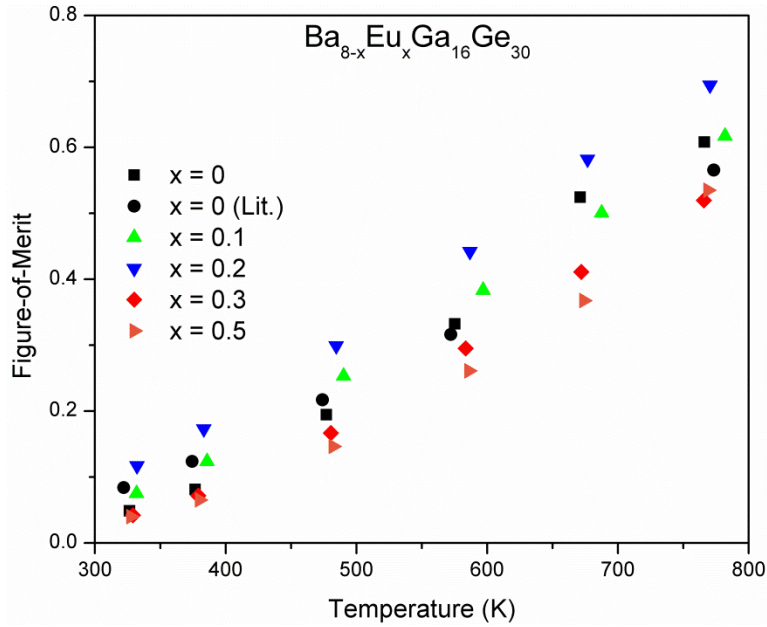


Figure 47: Figure-of-merit for Eu containing clathrates

Figure-of-merit for the sample with $x = 0$ at ~ 330 K is 0.05 which increases to 0.61 at ~ 780 K. The sample with $x = 0.3$ displays a figure-of-merit of 0.04 at ~ 330 K and 0.52 at ~ 780 K. For the sample with $x = 0.5$, it has a figure-of-merit of 0.04 at ~ 330 K and 0.53 at ~ 780 K. Samples with $x = 0.3$ and $x = 0.5$ have lower ZT than samples with $x = 0$. The sample with $x = 0.1$ has ZT of 0.07 at 330 K and at 780 K the ZT is 0.62. The sample with $x = 0.2$ displays the best ZT of all samples starting out at 0.12 at 330 K and increasing to 0.69 at 770 K.

The general trend for all samples is an increase in figure-of-merit with increasing temperature which is caused by increase in power factor and reduction in thermal conductivity.

5.5 Conclusion

Europium containing clathrates were investigated with the formula $\text{Ba}_{8-x}\text{Eu}_x\text{Ga}_{16}\text{Ge}_{30}$ with values of x ranging from 0 to 0.5. PXRD data suggested that $x = 0.5$ is the upper solubility limit for these clathrates. PXRD revealed phase pure samples after synthesis. However, after physical property measurements, side products such as Ge and BaGa_2 are present. EPMA and EDX data suggests that the atomic composition of the samples is close to expected results except for Eu which seems to be less than expected. This implies that the solubility limit is less than 0.5 per formula unit. The sample with $x = 0.5$ also shows the presence of europium oxide. The sample with $x = 0.2$ displayed the best ZT out of all samples with 0.69 at 770 K. This corresponds to a 13% improvement on the Eu free sample which displayed a ZT of 0.61 at 780 K.

6. Conclusion

The following double filled clathrates were synthesized during this project: $\text{Ba}_{8-x}\text{La}_x\text{Ga}_{16}\text{Ge}_{30}$ and $\text{Ba}_{8-x}\text{Eu}_x\text{Ga}_{16}\text{Ge}_{30}$. Synthesizing pure phase compounds was a challenge throughout the project.

PXRD was used for analysis of the double filled clathrates. After synthesis, PXRD revealed samples were phase pure when compared to literature $\text{Ba}_8\text{Ga}_{16}\text{Ge}_{30}$ sample. After hot pressing and physical property measurements, however, side products such as Ge and BaGa_2 start to appear in the samples.

For $\text{Ba}_{8-x}\text{Eu}_x\text{Ga}_{16}\text{Ge}_{30}$, $x = 0.5$ seemed to be the solubility limit based on PXRD analysis. Beyond $x = 0.6$, samples are no longer pure with BaGe_3 as the main side product.

Single crystal X-ray data on Eu containing clathrates revealed that Eu prefers the $6d$ Wyckoff position in the structure. The ADP of this site is almost 4 times higher than the ADP of the $2a$ site which suggests that Eu in $6d$ site acts as the rattler.

Addition of La causes reduction of thermal conductivity when compared to the $\text{Ba}_8\text{Ga}_{16}\text{Ge}_{30}$. Addition of Eu lowers the thermal conductivity up until $x = 0.2$ when compared to $\text{Ba}_8\text{Ga}_{16}\text{Ge}_{30}$. After which, the thermal conductivity is unaffected by additional Eu input.

Inclusion of La causes a decrease in electrical conductivity in general. This is more evident at higher temperatures. Addition of La seems to lower mobility which would explain the decrease in electrical conductivity. Inclusion of Eu decreases electrical conductivity up until $x = 0.2$. Beyond $x = 0.2$, Eu samples display similar electrical conductivity to the sample with $x = 0$. The decrease in electrical conductivity may be attributed to the decrease in mobility.

All double filled clathrates were *n*-type semiconductors with negative Seebeck coefficient values. Introducing La within the structure causes a slight increase in Seebeck coefficient although it is within error. Samples with $x = 0.1$ and $x = 0.2$ have higher Seebeck coefficient than $\text{Ba}_8\text{Ga}_{16}\text{Ge}_{30}$ while samples with $x = 0.3$ and $x = 0.5$ have lower Seebeck coefficient.

La inclusion might cause an increase in figure-of-merit of up to 8% which however is not a significant increase. $\text{Ba}_{7.9}\text{La}_{0.1}\text{Ga}_{16}\text{Ge}_{30}$ seems to be the best La containing sample. Eu inclusion causes an increase in figure-of-merit up to 13%. $\text{Ba}_{7.8}\text{Eu}_{0.2}\text{Ga}_{16}\text{Ge}_{30}$ seems to be best Eu containing clathrate with a *ZT* of 0.69 at 770 K. Compared to the best literature Czochralski pulled clathrate, which displayed a *ZT* of 1.1 at 800 K, these results are a bit lacking. The Eu and Ba filled clathrate if synthesized using the Czochralski pulled method may increase the *ZT* as well. The results presented here show that double filled clathrates are potential materials for thermoelectric applications. Further studies in double substitution as well as host atom substitutions are required.

References

- (1) Kleinke, H. *Chem. Mater.* 2010, 22, 604.
- (2) Winder, E. J.; Ellis, A. B.; Lisensky, G. C. *J. Chem. Edu.* 1996, 73, 940.
- (3) Snyder, G. J.; Toberer, E. S. *Nat. Mater.* 2008, 7, 105.
- (4) Bell, L. E. *Science* 2008, 321, 1457.
- (5) Rowe, D. M. *CRC Handbook of Thermoelectrics*; CRC Press: Boca Raton, FL, 1995.
- (6) Kuropatwa, B. A., "Exploration and Optimization of Tellurium-Based Thermoelectrics" University of Waterloo, 2012.
- (7) Tritt, T. M.; Subramanian, M. *MRS Bull.* 2006, 31, 188.
- (8) Snyder, G. J.; Caillat, T. In *Mater. Res. Soc. Sym. Proc.*; Cambridge Univ Press: 2004; Vol. 793, p 37.
- (9) Karamitaheri, H., "Thermal and Thermoelectric Properties of Nanostructures", Technical University of Vienna, 2013.
- (10) May, A. F.; Toberer, E. S.; Saramat, A.; Snyder, G. J. *Phys. Rev. B* 2009, 80, 125205.
- (11) Fistul', V. I. *Heavily Doped Semiconductors*; Plenum Press: New York, 1969.
- (12) Dughaish, Z. *Physica B: Cond. Mat.* 2002, 322, 205.
- (13) Angrum, A. In *Voyager: The Interstellar Mission*; Vol. 2014.
- (14) Zhao, X.; Ji, X.; Zhang, Y.; Zhu, T.; Tu, J.; Zhang, X. *Appl. Phys. Lett.* 2005, 86, 062111.
- (15) Tang, X.; Xie, W.; Li, H.; Zhao, W.; Zhang, Q.; Niino, M. *Appl. Phys. Lett.* 2007, 90, 012102.
- (16) LaLonde, A. D.; Pei, Y.; Wang, H.; Snyder, G. J. *Mater. Today* 2011, 14, 526.
- (17) Jeffrey, Snyder, G. *Energ. Environ. Sci.* 2011, 4, 2085.
- (18) Jeffrey, Snyder, G. *Energ. Environ. Sci.* 2011, 4, 2090.
- (19) Biswas, K.; He, J.; Blum, I. D.; Wu, C.-I.; Hogan, T. P.; Seidman, D. N.; Dravid, V. P.; Kanatzidis, M. G. *Nature* 2012, 489, 414.
- (20) Kurosaki, K.; Yamanaka, S. *Phys. Status Solidi A*, 2013, 210, 82.
- (21) Sharp, J. W.; Sales, B. C.; Mandrus, D. G.; Chakoumakos, B. C. *Appl. Phys. Lett.* 1999, 74, 3794.
- (22) Wölfing, B.; Kloc, C.; Teubner, J.; Bucher, E. *Phys. Rev. Lett.* 2001, 86, 4350.
- (23) Guo, Q.; Assoud, A.; Kleinke, H. *Adv. Energy Mater.* 2014, 4, 1400348.
- (24) Slack, G. A. *CRC Handbook of Thermoelectrics* 1995, 407.
- (25) He, Y.; Day, T.; Zhang, T.; Liu, H.; Shi, X.; Chen, L.; Snyder, G. J. *Adv. Mater.* 2014, 26, 3974.
- (26) Liu, H.; Shi, X.; Xu, F.; Zhang, L.; Zhang, W.; Chen, L.; Li, Q.; Uher, C.; Day, T.; Snyder, G. *J. Nat. Mater.* 2012, 11, 422.
- (27) Brown, D. R.; Day, T.; Caillat, T.; Snyder, G. J. *J. Electron. Mater.* 2013, 42, 2014.
- (28) Oudah, M.; Kleinke, K. M.; Kleinke, H. *Inorg. Chem.* 2014, 54, 845.
- (29) Yang, J.; Caillat, T. *MRS Bull.* 2006, 31, 224.
- (30) Nolas, G.; Kaeser, M.; Littleton IV, R.; Tritt, T. *Appl. Phys. Lett.* 2000, 77, 1855.
- (31) Puyet, M.; Dauscher, A.; Lenoir, B.; Dehmas, M.; Stiewe, C.; Müller, E.; Hejtmanek, J. *J. Appl. Phys.* 2005, 97, 083712.
- (32) Zhao, W.; Dong, C.; Wei, P.; Guan, W.; Liu, L.; Zhai, P.; Tang, X.; Zhang, Q. *J. Appl. Phys.* 2007, 102, 113708.
- (33) Chen, L.; Kawahara, T.; Tang, X.; Goto, T.; Hirai, T.; Dyck, J. S.; Chen, W.; Uher, C. *J. Appl. Phys.* 2001, 90, 1864.

- (34) Sum, A. K.; Koh, C. A.; Sloan, E. D. *Ind. Eng. Chem. Res.* 2009, *48*, 7457.
- (35) Karttunen, A. J.; Fässler, T. F.; Linnolahti, M.; Pakkanen, T. A. *Inorg. Chem.* 2010, *50*, 1733.
- (36) Deng, S.; Saiga, Y.; Suekuni, K.; Takabatake, T. *J. Appl. Phys.* 2010, *108*, 073705.
- (37) Kim, J.-H.; Okamoto, N. L.; Kishida, K.; Tanaka, K.; Inui, H. *Acta Mater.* 2006, *54*, 2057.
- (38) Christensen, M.; Johnsen, S.; Iversen, B. B. *Dalton Trans.* 2010, *39*, 978.
- (39) Leoni, S.; Carrillo-Cabrera, W.; Grin, Y. *J. Alloy Compd.* 2003, *350*, 113.
- (40) Du, B.; Saiga, Y.; Kajisa, K.; Takabatake, T.; Nishibori, E.; Sawa, H. *Philos. Mag.* 2012, *92*, 2541.
- (41) Nolas, G.; Cohn, J.; Slack, G.; Schujman, S. *Appl. Phys. Lett.* 1998, *73*, 178.
- (42) Cao, W.-Q.; Yan, Y.-G.; Tang, X.-F.; Deng, S.-K. *J. Phys. D Appl. Phys.* 2008, *41*, 215105.
- (43) Fujita, I.; Kishimoto, K.; Sato, M.; Anno, H.; Koyanagi, T. *J. Appl. Phys.* 2006, *99*, 093707.
- (44) Kuznetsov, V. L.; Kuznetsova, L. A.; Kaliazin, A. E.; Rowe, D. M. *J. Appl. Phys.* 2000, *87*, 7871.
- (45) Cederkrantz, D.; Nygren, M.; Palmqvist, A. *J. Appl. Phys.* 2010, *108*, 113711.
- (46) Okamoto, N. L.; Kishida, K.; Tanaka, K.; Inui, H. *J. Appl. Phys.* 2007, *101*, 113525.
- (47) Heijl, R.; Cederkrantz, D.; Nygren, M.; Palmqvist, A. *J. Appl. Phys.* 2012, *112*, 044313.
- (48) Anno, H.; Hokazono, M.; Kawamura, M.; Nagao, J.; Matsubara, K. In *Thermoelectrics, 2002. Proceedings ICT'02. Twenty-First International Conference on*; IEEE: 2002, p 77.
- (49) Toberer, E. S.; Christensen, M.; Iversen, B. B.; Snyder, G. J. *Phys. Rev. B* 2008, *77*, 075203.
- (50) Deng, S.; Tang, X.; Li, P.; Zhang, Q. *J. Appl. Phys.* 2008, *103*, 073503.
- (51) Shi, X.; Yang, J.; Bai, S.; Yang, J.; Wang, H.; Chi, M.; Salvador, J. R.; Zhang, W.; Chen, L.; Wong-Ng, W. *Adv. Funct. Mater.* 2010, *20*, 755.
- (52) Hou, X.; Zhou, Y.; Wang, L.; Zhang, W.; Zhang, W.; Chen, L. *J. Alloy. Compd.* 2009, *482*, 544.
- (53) Saramat, A.; Svensson, G.; Palmqvist, A. E. C.; Stiewe, C.; Mueller, E.; Platzek, D.; Williams, S. G. K.; Rowe, D. M.; Bryan, J. D.; Stucky, G. D. *J. Appl. Phys.* 2006, *99*, 023708/1.
- (54) Cohn, J.; Nolas, G.; Fessatidis, V.; Metcalf, T.; Slack, G. *Phys. Rev. Lett.* 1999, *82*, 779.
- (55) Tang, X.; Li, P.; Deng, S.; Zhang, Q. *J. Appl. Phys.* 2008, *104*, 013706.
- (56) Paschen, S.; Gspan, C.; Grogger, W.; Dienstleder, M.; Laumann, S.; Pongratz, P.; Sassik, H.; Wernisch, J.; Prokofiev, A. *J. Cryst. Growth* 2008, *310*, 1853.
- (57) Yan, X.; Chen, M.; Laumann, S.; Bauer, E.; Rogl, P.; Podloucky, R.; Paschen, S. *Phys. Rev. B* 2012, *85*, 165127.
- (58) Deng, S.; Tang, X.; Li, P.; Zhang, Q. *J. Appl. Phys.* 2008, *103*, 073503.
- (59) Electron Microprobe Laboratory, University of Arizona.
http://pirlwww.lpl.arizona.edu/~domanik/UA_Microprobe/Intro.html 2015.
- (60) JEOL USA, Inc: 2015; <http://www.jeolusa.com/PRODUCTS/MicroprobeandAuger/JXA8230/tabid/223/Default.aspx> 2015.
- (61) Sales, B.; Chakoumakos, B.; Jin, R.; Thompson, J.; Mandrus, D. *Phys. Rev. B* 2001, *63*, 245113.